Ocean biogeochemistry in the Canadian Earth System Model version 5.0.3: CanESM5 and CanESM5-CanOE

James R. Christian[1,2], Kenneth L. Denman[2,3], Hakase Hayashida[3,4], Amber M. Holdsworth[1], Warren G. Lee[2], Olivier G.J. Riche[3,5], Andrew E. Shao[2,3], Nadja Steiner[1,2], and Neil C. Swart[2]

1 Fisheries and Oceans Canada, Sidney, BC, Canada

2 Canadian Centre for Climate Modelling and Analysis, Victoria, BC, Canada

3 School of Earth and Ocean Sciences, University of Victoria, Victoria, BC, Canada

4 now at the Institute for Marine and Antarctic Studies, University of Tasmania, Hobart, Tasmania, Australia

5 now at Fisheries and Oceans Canada, Mont Joli, Québec, Canada

Correspondence to: jim.christian@ec.gc.ca

Abstract. The ocean biogeochemistry components of two new versions of the Canadian Earth

System Model are presented and compared to observations and other models. CanESM5

employs the same ocean biology model as CanESM2 whereas CanESM5-CanOE ("Canadian

Ocean Ecosystem model") is a new, more complex model developed for CMIP6, with multiple

food chains, flexible phytoplankton elemental ratios, and a prognostic iron cycle. This new

model is described in detail and the outputs (distributions of major tracers such as oxygen,

dissolved inorganic carbon, and alkalinity, the iron and nitrogen cycles, plankton biomass, and

historical trends in CO_2 uptake and export production) compared to CanESM5 and CanESM2, as

well as to observations and other CMIP6 models. Both CanESM5 models show gains in skill

relative to CanESM2, which are attributed primarily to improvements in ocean circulation.

CanESM5-CanOE shows improved skill relative to CanESM5 for most major tracers at most

depths. CanESM5-CanOE includes a prognostic iron cycle, and maintains high nutrient / low

chlorophyll conditions in the expected regions (in CanESM2 and CanESM5, iron limitation is

specified as a temporally static 'mask'). Surface nitrate concentrations are biased low in the

subarctic Pacific and equatorial Pacific, and high in the Southern Ocean, in both CanESM5 and

CanESM5-CanOE. Export production in CanESM5-CanOE is among the lowest for CMIP6

models; in CanESM5 it is among the highest, but shows the most rapid decline after about 1980.

CanESM5-CanOE shows some ability to simulate aspects of plankton community structure that a

single-species model can not (e.g., seasonal dominance of large cells), but is biased towards low

concentrations of zooplankton and detritus relative to phytoplankton. Cumulative ocean uptake

of anthropogenic carbon dioxide through 2014 is lower in both CanESM5-CanOE (122 PgC) and

CanESM5 (132 PgC) than in observation-based estimates (145 PgC) or the model ensemble

mean (144 PgC)..

1. **Introduction**

The Canadian Centre for Climate Modelling and Analysis has been developing coupled models with an interactive carbon cycle for more than a decade (Christian et al., 2010; Arora et al., 2011). The Canadian Earth System Model version 5 (CanESM5, Swart et al., 2019a) is an updated version of CanESM2 (Arora et al., 2011), with a new ocean model based on the Nucleus for European Modelling of the Ocean (NEMO) system version 3.4. The ocean biogeochemistry modules were developed in-house. CanESM5 uses the same ocean biology model as CanESM1 (Christian et al., 2010) and CanESM2 (Arora et al., 2011), the Canadian Model of Ocean Carbon (CMOC; Zahariev et al., 2008). An additional model was developed for CMIP6, called the Canadian Ocean Ecosystem model (CanOE). The biological components of CanOE are of substantially greater complexity than CMOC, including multiple food chains, flexible phytoplankton elemental ratios, and a prognostic iron (Fe) cycle. The two coupled models are known as CanESM5 and CanESM5-CanOE, respectively.

The reasons for developing both models are, firstly, to evaluate the effect of changes in ocean circulation between CanESM2 and CanESM5 on ocean biogeochemistry by running the new climate model with the same ocean biogeochemistry, and secondly because CanOE is substantially more expensive computationally (19 tracers vs 7, so the total computation time to integrate the ocean model with biogeochemistry is approximately double). Most CMIP6 experiments were run with CanESM5 only, as ocean biogeochemistry is not central to their purpose. Additional tracers requested by the Ocean Model Intercomparison Project - Biogeochemistry (OMIP-BGC) including abiotic and natural dissolved inorganic carbon (DIC),

66   DI^{14}C, CFCs and SF$_6$ (see Orr et al., 2017) were run only in CanESM5. The CMIP6 experiments

67   published for CanESM5-CanOE are listed in Supplementary Table S1.

69   CMOC is a nutrient-phytoplankton-zooplankton-detritus (NPZD) model with highly

70   parameterized representations of phytoplankton Fe limitation, dinitrogen (N$_2$) fixation and

71   denitrification, and calcification and calcite dissolution (Zahariev et al., 2008; Supplementary

72   Figure S1). CanESM1 and CanESM2 did not include oxygen;CanESM5 includes oxygen as a

73   purely 'downstream' tracer that does not affect other biogeochemical processes. In CanESM5-

74   CanOE, denitrification is prognostic and dependent on the concentration of oxygen. Among the

75   less satisfactory aspects of CMOC biogeochemistry are, firstly, that Fe limitation is specified as a

76   static 'mask' that does not change with climate (it is calculated from the present-day

77   climatological distribution of nitrate, based on the assumption that regions without iron

78   limitation will have complete drawdown of surface nitrate at some point in the year), and

79   secondly, that denitrification is parameterized so that nitrogen (N) is conserved within each

80   vertical column, i.e., collocated with N$_2$ fixation in tropical and subtropical open-ocean regions

81   (Zahariev et al., 2008; Riche and Christian, 2018). This latter simplification produced excessive

82   accumulations of nitrate in Eastern Boundary Current (EBC) regions where most denitrification

83   occurs. CMOC also has a tendency to produce rather stark extremes of high and low primary and

84   export production (Zahariev et al., 2008), a well-known problem of NPZD models (Armstrong,

85   1994; Friedrichs et al., 2007). Our intent in developing CanOE was to alleviate, or at least

86   reduce, these biases, by including multiple food chains, a prognostic Fe cycle, and prognostic

87   denitrification. Dinitrogen fixation is still parameterized, but the CanOE parameterization

88   includes Fe (but not P) limitation, whereas in CMOC N$_2$ fixation tends to grow without bound in

89   a warming ocean as CMOC does not include P or Fe limitation (Riche and Christian, 2018).

90

91   In this paper we present a detailed model description for CanOE and an evaluation of both

92   CanESM5 and CanESM5-CanOE relative to observational data products and other available

93   models. CMOC has been well described previously (Zahariev et al., 2008) and the details are not

94   reiterated here. In some cases, CanESM2 results are also shown to illustrate which differences in

95   the model solutions arise largely from the evolution of the physical climate model, and which are

96   specifically associated with different representations of biogeochemistry. An overall evaluation

97   of the CanESM5 climate including the physical ocean is given in Swart et al. (2019a). Here, we

98   focus on biogeochemical variables, and have evaluated model performance in three main areas:

99   (1) the distribution of major tracers like oxygen, DIC and alkalinity, and the resulting saturation

100   state for $CaCO_3$ minerals, (2) the iron cycle and its interaction with the nitrogen cycle, and (3)

101   plankton community structure and the concentration and export of particulates. We first address

102   the major chemical species that are common to both models (and almost all other Earth System

103   Models) to determine whether a more complex biology model measurably improves skill, and

104   whether the updated circulation model improves skill relative to CanESM2. Then we examine

105   the areas where our two models differ: the presence of a prognostic iron cycle and multiple food

106   chains in CanOE. More specifically, does CanESM5-CanOE reproduce the geographic

107   distribution of High-Nutrient, Low-Chlorophyll (HNLC) regions? Does the large phytoplankton /

108   large zooplankton food chain become dominant under nutrient-rich conditions, and how does

109   having multiple detrital size classes affect particle flux and remineralization length scale?

110   Following this model evaluation, we present historical trends in ocean anthropogenic CO_2

111   uptake, export production, and total volume of low-oxygen waters over the historical (1850-

112   2014) experiment. Possible future changes under Shared Socioeconomic Pathway experiments

113   will be addressed in subsequent publications.

114

115   **2. Model Description**

116

117   CanESM5 (Swart et al., 2019a) is an updated version of CanESM2 (Arora et al., 2011), with an

118   entirely new ocean. The atmosphere model has the same T63 horizontal resolution, and contains

119   some important improvements in atmospheric physics (Swart et al., 2019a). The land surface

120   (Canadian Land Surface Scheme) and terrestrial carbon cycle (Canadian Terrestrial Ecosystem

121   Model) models are substantially the same as in CanESM2 with minor modifications as described

122   by Arora et al. (2020). The CanESM5 ocean is based on the NEMO modelling system version

123   3.4, with a horizontal resolution of 1°, telescoping to 1/3° in the tropics, and 45 vertical levels

124   ranging in thickness from ~6 m near the surface to ~250 m in the deep ocean (Swart et al.,

125   2019a). All physical climate model components are the same in CanESM5 and CanESM5-

126   CanOE. There are no feedbacks between biology and the physical ocean model, so the physical

127   climate of CanESM5 and CanESM5-CanOE is identical in experiments with prescribed

128   atmospheric CO_2 concentration.

129

130   The NEMO system is a publicly available archive of codes based on the OPA (Océan

131   PArallelisé) ocean model (Madec and Imbard, 1996; Guilyardi and Madec, 1997) and the

132   Tracers in Ocean Paradigm (TOP) module for tracer advection and mixing. Our ocean

133   biogeochemistry modules are built within TOP, using NEMO v3.4.1, but have also been

134   implemented in NEMO 3.6 for regional downscaling applications (Holdsworth et al., 2021).

135

Carbon chemistry is based on the Best Practices Guide (Dickson et al., 2007) and the OMIP-

BGC data request (Orr et al., 2017) and are identical in CanESM5 and CanESM5-CanOE. All

calculations are done on the total scale and the recommended formulae for the equilibrium

constants are employed. The carbon chemistry solver was run for a fixed number of iterations

(ten in the surface layer, and five in the subsurface layers in CanESM5-CanOE). CanESM5 does

not solve the carbon chemistry equations in the subsurface layers. OMIP-BGC formulations for

CO_2 and O_2 solubility and gas exchange are employed. It is important to note here that the

carbon chemistry and gas exchange formulations used in CanESM2 (and other CMIP5 models)

are slightly different than those used in CMIP6. However, this difference is of little functional

significance, i.e., it will have a negligible impact on the distribution of $[CO3^{--}]$ compared to the

differences in DIC and alkalinity distribution. The initialization fields for nitrate, DIC and

alkalinity were also different in CanESM2. This will affect the total ocean inventory of DIC but

not the spatial distribution if the model is well equilibrated.

149

The CanOE biology model is based on the cellular regulation model of Geider et al. (1998).

There are two phytoplankton size classes, and each group has four state variables: C, N, Fe and

chlorophyll. Photosynthesis is decoupled from cell production and photosynthetic rate is a

function of the cell's internal N and Fe quotas. Each functional group has a specified minimum

and maximum N quota and Fe quota, and nutrient uptake ceases when the maximal cell quota is

reached. Chlorophyll synthesis is a function of N uptake and increases at low irradiance. There

are also two size classes each of zooplankton and detritus. Small zooplankton graze on small

157 phytoplankton, while large zooplankton graze on both large phytoplankton and small

158 zooplankton. Small detritus sinks at 2 m d^{-1} and large detritus at 30

159 m d^{-1} (in CanESM5 there is a single detrital pool with a sinking rate of 8 m d^{-1}). Model

160 parameters and their values are listed in Table 1. A schematic of the model is shown in Figure 1.

161

162 **2.1 Photosynthesis and Phytoplankton Growth**

163

164 For simplicity and clarity, the equations are shown here for a single phytoplankton species, and

165 do not differ structurally for small and large phytoplankton. Some parameter values differ for the

166 two phytoplankton groups; all parameter values are listed in Table 1.

167

168 Temperature dependence of photosynthetic activity is expressed by the Arrhenius equation

169 $$T_f = \exp\left(-\frac{E_{ap}}{R}\left(\frac{1}{T} - \frac{1}{T_{\text{ref}}}\right)\right) \tag{1}$$

170 where E_{ap} is an enzyme activation energy that corresponds approximately to that of RuBisCo (cf.

171 Raven and Geider 1988), R is the gas constant (8.314 J mol^{-1} K^{-1}), and temperature T and

172 reference temperature T_{ref} are in Kelvin. Maximal rates of nutrient (either N or Fe, but

173 generically referred to here with the superscript X) uptake are given by

174 $$V_{max}^X = V_{ref}^X T_f \left(\frac{Q_{max}^X - Q^X}{Q_{max}^X - Q_{min}^X}\right)^{0.05} \tag{2}$$

175 where V_{max}^X is the maximal uptake rate in mg of nutrient X per mg of cell C, X can represent N

176 or Fe, Q is the nutrient cell quota and Q_{min} and Q_{max} its minimum and maximum values, and V_{ref}^X

177 is a (specified) basal rate at $T=T_{ref}$ and $Q=Q_{min}$. These maximum rates are then reduced according

178 to the ambient nutrient concentration, i.e.
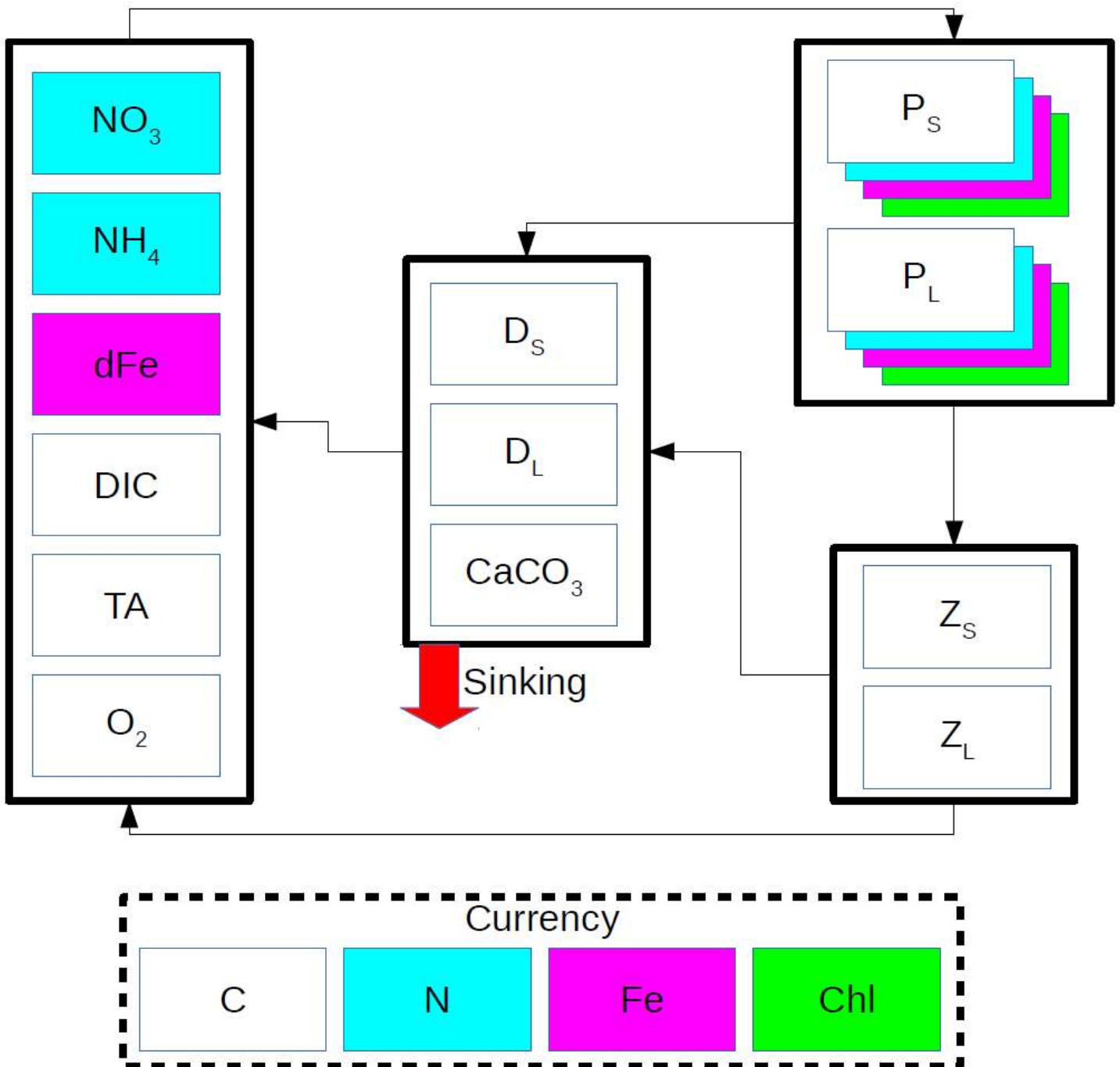
Figure 1 - Schematic of the CanOE biology model. Model currencies including chlorophyll (Chl) are indicated by coloured boxes except oxygen (O_2) and carbonate ($CaCO_3$). Arrows indicate flows of carbon (C), nitrogen (N) and iron (Fe) between compartments containing small (S) and large (L) phytoplankton (P), zooplankton (Z), and detritus (D) components; counterflows of oxygen are not shown.

Table 1 – Ecosystem model parameters.

Symbol	Description	Unit	
T_{ref}	Reference temperature	K	298.15
E_{ap}	Activation energy for photosynthesis	kJ mol^{-1}	37.4
Q^N_{mins}	Small phytoplankton minimum N quota	g N g C^{-1}	0.04
Q^N_{maxs}	Small phytoplankton maximum N quota	g N g C^{-1}	0.172
Q^N_{minl}	Large phytoplankton minimum N quota	g N g C^{-1}	0.04
Q^N_{maxl}	Large phytoplankton maximum N quota	g N g C^{-1}	0.172
Q^{Fe}_{mins}	Small phytoplankton minimum Fe quota	µg Fe g C^{-1}	4.65
Q^{Fe}_{maxs}	Small phytoplankton maximum Fe quota	µg Fe g C^{-1}	93.
Q^{Fe}_{minl}	Large phytoplankton minimum Fe quota	µg Fe g C^{-1}	6.5
Q^{Fe}_{maxl}	Large phytoplankton maximum Fe quota	µg Fe g C^{-1}	70.
V^N_{ref}	Reference rate of N uptake	g N g C^{-1} d^{-1}	0.6
V^{Fe}_{ref}	Reference rate of Fe uptake	µg Fe g C^{-1} d^{-1}	79.
P^C_{ref}	Reference rate of photosynthesis	g C g C^{-1} d^{-1}	3
k_{XU}	Rate coefficient for exhudation	d^{-1}	1.7
k_{dgr}	Rate coefficient for chlorophyll degradation	d^{-1}	0.02
ζ	Respiratory cost of biosynthesis	g C g N^{-1}	2
α_{chl}	Initial slope of P-E curve	g C g CHL^{-1} h^{-1} (µmol m^{-2} s^{-1})$^{-1}$	1.08
Θ^N_{max}	Maximum chlorophyll-nitrogen ratio	g g^{-1}	0.18
K_{NiS}	Half-saturation for small phytoplankton nitrate uptake	mmol^{-1} m^3	0.1
K_{NaS}	Half-saturation for small phytoplankton ammonium uptake	mmol^{-1} m^3	0.05
K_{FeS}	Half-saturation for small phytoplankton iron uptake	nmol^{-1} m^3	100
K_{NiL}	Half-saturation for large phytoplankton nitrate uptake	mmol^{-1} m^3	1.0
K_{NaL}	Half-saturation for large phytoplankton ammonium uptake	mmol^{-1} m^3	0.05
K_{FeL}	Half-saturation for large phytoplankton iron uptake	nmol^{-1} m^3	200
m_{1S}	Small phytoplankton/zooplankton mortality rate (linear)	d^{-1}	0.05
m_{2S}	Small phytoplankton/zooplankton mortality coefficient	(mmol C m^{-3})$^{-1}$ d^{-1}	0.06
m_{1L}	Large phytoplankton/zooplankton mortality rate (linear)	d^{-1}	0.1

m_{2L}	Large phytoplankton/zooplankton mortality coefficient	(mmol C m^{-3})$^{-1}$ d^{-1}	0.06
X_{minp}	Minimum phytoplankton concentration for linear mortality	mmol C m^{-3}	0.01
a_L	Large zooplankton grazing parameter	(mmol C m^{-3})$^{-1}$	0.25
G_{L0}	Large zooplankton maximum grazing rate	d^{-1}	0.85
a_S	Small zooplankton grazing parameter	(mmol C m^{-3})$^{-1}$	0.25
G_{S0}	Small zooplankton maximum grazing rate	d^{-1}	1.7
λ	Assimilation efficiency	n.d.	0.8
r_{zs}	Microzooplankton specific respiration rate at T_{ref}	d^{-1}	0.3
r_{zl}	Mesozooplankton specific respiration rate at T_{ref}	d^{-1}	0.1
r_1	Small detritus remineralization rate at T_{ref}	d^{-1}	0.25
r_2	Large detritus remineralization rate at T_{ref}	d^{-1}	0.25
E_{ar}	Activation energy for detritus remineralization	kJ mol^{-1}	54.0
w_s	Small detritus sinking speed	m d^{-1}	2.
w_l	Large detritus sinking speed	m d^{-1}	30.
w_{Ca}	CaCO$_3$ sinking speed	m d^{-1}	20.
P_{Ca}	CaCO$_3$ production as fraction of mortality	mol CaCO$_3$ molC^{-1}	0.05
k_{Ca}	CaCO$_3$ dissolution rate	d^{-1}	0.0074
S_{Fe1}	Dissolved iron scavenging loss rate (Fe≤L$_{Fe}$)	d^{-1}	0.001
S_{Fe2}	Dissolved iron scavenging loss rate (Fe>L$_{Fe}$)	d^{-1}	2.5
L_{Fe}	Ligand concentration	nmol Fe m^{-3}	600.
P_{Fe}	POC-dependence parameter for Fe scavenging	(mmolC m^{-3})$^{-1}$	0.66
k_{NH4ox}	Nitrification rate constant	d^{-1}	0.05
K_E	Half-saturation for irradiance inhibition of nitrification	W m^{-2}	1.
k_{dnf}	Light and nutrient saturated rate of N$_2$ fixation at 30°C	mmol N m^{-3} d^{-1}	0.0225
a	Initial slope for irradiance-dependence of N$_2$ fixation	(W m^{-2})$^{-1}$	0.02
K_{Fe}	Half-saturation for Fe dependence of N$_2$ fixation	nmol Fe m^{-3}	100.
K_{NO3}	Half-saturation for DIN inhibition of N$_2$ fixation	mmol m^{-3}	0.1
O_{mxd}	O$_2$ concentration threshold for denitrification	mmol m^{-3}	6.
A_f	Anammox fraction of N loss to denitrification	n.d.	0.25

182     $V^N = V_{max}^N(L_{NH4} + (1 - L_{NH4})L_{NO3})$ (3a)

183   where $L_{\text{NH4}} = \dfrac{N_a}{K_{\text{NaX}}+N_a}$ and $L_{\text{NO3}} = \dfrac{N_i}{K_{\text{NiX}}+N_i}$, with N_i and N_a indicating nitrate and ammonium

184   respectively, and

185     $V^{Fe} = V_{max}^{Fe} \left(\dfrac{\text{Fe}}{K_{\text{FeX}}+\text{Fe}} \right)$ (3b)

186   where X indicates large or small phytoplankton (Table 1). The maximal carbon-based growth

187   rate is given by

188     $P_{max}^C = P_{ref}^C T_f \min\{\dfrac{Q^N - Q_{min}^N}{Q_{max}^N - Q_{min}^N} \cdot \dfrac{Q^{Fe} - Q_{min}^{Fe}}{Q_{max}^{Fe} - Q_{min}^{Fe}}\}$ (4)

189   where P^C_{ref} is the rate at the reference temperature T_{ref} under nutrient-replete conditions

190   ($Q=Q_{max}$). The light-limited growth rate is then given by

191     $P_{phot}^C = P_{max}^C \left(1 - e^{-\alpha_{chl}E\theta_C \big/ P_{max}^C} \right)$ (5)

192   where E is irradiance and θ_C is the chlorophyll-to-carbon ratio. The rate of chlorophyll synthesis

193   is

194     $\rho_{\text{chl}} = \theta_{max}^N \dfrac{P_{phot}^C}{E\alpha_{\text{chl}}\theta}$ (6)

195   These rates are then used to define a set of state equations for phytoplankton carbon (C_p),

196   nitrogen (N_p), iron (Fe_p), and chlorophyll (M).

197     $\frac{dC_p}{dt} = (P_{phot}^C - \zeta V_N)C_p - (G + C_{XS}) - m_1 C_p - m_2 C_p^2 - k_{\text{XU}}C_{\text{INTR}}$ (7)

198   where ζ is the respiratory cost of biosynthesis, G is the grazing rate (equation 12), C_{XS} is the

199   excess (above the ratio in grazer biomass) carbon in grazing losses (see below equation 16a), m_1

200   and m_2 are coefficients for linear and quadratic nonspecific mortality terms, C_{INTR} is the

201   concentration of intracellular carbohydrate carbon in excess of biosynthetic requirements, and

202   k_{XU} is a rate coefficient for its exudation to the environment. The nonspecific mortality terms are

203   set to 0 below 0.01 mmol C m^{-3}, to prevent biomass from being driven to excessively low levels

204   in the high latitudes in winter; linear mortality terms can result in biomass declining to levels

205   from which recovery would take much longer than the brief Arctic summer (Hayashida, 2018).

206   The full equation for phytoplankton N, Fe and chlorophyll are

207     $$\frac{dN_p}{dt} = \frac{V^N}{Q_N} - (G + m_1 C_p + m_2 C_p^2) R_{NC} - N_{XS} \tag{8}$$

208     $$\frac{dFe_p}{dt} = \frac{V^{Fe}}{Q_{Fe}} - (G + m_1 C_P + m_2 C_p^2) R_{FeC} - Fe_{XS} \tag{9}$$

209     $$\frac{dM}{dt} = \frac{\rho_{chl} V^N}{\theta_C} M - (G + m_1 C_p + m_2 C_p^2) \theta_C - k_{dgr} M \tag{10}$$

210   where k_{dgr} is a rate coefficient for nonspecific losses of chlorophyll e.g., by photooxidation, in

211   addition to losses to grazing and other processes that also affect C_p, N_p, and Fe_p. N_{XS} and Fe_{XS} are

212   remineralization of "excess" (relative to grazer or detritus ratios) N or Fe and are defined below

213   (equation 16).

214

215   **2.2 Grazing and Food Web Interactions**

216

217   Grazing rate depends on the phytoplankton carbon concentration, which most closely represents

218   the food concentration available to the grazer (Elser and Urabe 1999; Loladze et al. 2000).

219   Zooplankton biomass is also in carbon units. State equations for small and large zooplankton are

220     $$\frac{dZ_S}{dt} = \lambda G_S - (R + G_Z + m_{1s} Z_s + m_{2s} Z_s^2) \tag{11a}$$

221     $$\frac{dZ_L}{dt} = \lambda G_L - (R + m_{1L} Z_L + m_{2L} Z_L^2) \tag{11b}$$

222   where

223     $G_S = G_{so}(1 - e^{-a_s C_{ps}})Z_S$ (12a)

224     $G_L = G_{L0}(1 - e^{-a_l(C_{pl}+Z_s)})Z_L$ (12b)

225   for small and large zooplankton respectively, G_Z is grazing of small zooplankton by large

226   zooplankton, R is respiration, and m_1 and m_2 are nongrazing mortality rates. Large zooplankton

227   grazing is divided into grazing on large phytoplankton and small zooplankton in proportion to

228   the relative abundance of each

229     $G_P = G_L \frac{P_l}{P_l + Z_s}$ (13a)

230     $G_Z = G_L \frac{Z_s}{P_l + Z_s}$ (13b)

231   Zooplankton biomass loss to respiration is given by

232     $R = max\{r_z T_f Z - C_{XS}.0\}$ (14)

233   and uses the same activation energy as photosynthesis. Respiration (R) is assumed to consume

234   only carbon and not result in catabolism of existing biomass when "excess" carbon is available

235   in the prey. In addition, conservation of mass must be maintained by recycling to the dissolved

236   pool grazer consumption of elements in excess of biosynthetic requirements when grazer and

237   prey elemental ratios differ. In the case where the nutrient quota (relative to carbon) exceeds the

238   grazer fixed ratio, the excess nutrient is remineralized to the dissolved inorganic pool. In the case

239   where the nutrient quota is less than the grazer ratio, the grazer intake is reduced to what can be

240   supported by the least abundant nutrient (relative to the grazer biomass ratio) and excess carbon

241   is remineralized. For the case of two nutrients (in this case N and Fe) it is necessary to define

242     $G' = G \min \left\{ \frac{N_P}{C_P} R_{CN}, \frac{Fe_P}{C_P} R_{CFe}, 1 \right\}$ (15)

 where G is equal to G_S (equation 12a) for small zooplankton and G_P (equation 13a) for large

zooplankton, and R_{XY} indicates the fixed ratio of element X to element Y in grazer biomass. The

'excess' carbon available for respiration is

$$C_{XS} = G'\left\{\frac{C_P}{N_P}R_{NC} - 1, \frac{C_P}{Fe_P}R_{FeC} - 1, 0\right\} \tag{16a}$$

and the excess nutrients remineralized to their inorganic pools are

$$N_{XS} = G'\max\left\{\frac{N_P}{C_P} - R_{NC}.0\right\}\varepsilon + G'\max\left\{R_{NC}\left(\frac{N_P}{Fe_P}R_{FeN} - 1\right).0\right\}(1 - \varepsilon) \tag{16b}$$

$$Fe_{XS} = G'\max\left\{\frac{Fe_P}{C_P} - R_{FeC}.0\right\}\varepsilon + G'\max\left\{R_{FeC}(\frac{Fe_P}{N_P}R_{NFe} - 1).0\right\}(1 - \varepsilon) \tag{16c}$$

where

$$\varepsilon = \frac{\max\{C_{xs}, 0\}}{C_{xs} + \Delta}$$

is a switch to prevent double-counting in cases where one of the terms is redundant (the excess

relative to the least abundant element is included in the other term), but would otherwise be

nonzero (Δ is a constant equal to 10^{-15}, to prevent divide-by-zero). For three elements, there are

$3! = 6$ possible cases: for N greater or less than $C_P R_{NC}$, Fe may be either in excess relative to

both C and N, deficient relative to both, or in excess relative to one but not the other (Table 2).

Table 2 - Cases where the 'excess' terms are nonzero. These terms are always greater than or equal to zero, and always zero when the phytoplankton elemental ratio is equal to the grazer biomass ratio. A plus (+) sign indicates that a specific term is positive. N_1 and N_2, Fe_1 and Fe_2 indicate the first and second terms in equations 16b and 16c. R_{NC} is the grazer N/C (Redfield) ratio.

	Fe in excess relative to both C and N					Fe in excess relative to C or N but not both					Fe deficient relative to both C and N				
	C	N_1	N_2	Fe_1	Fe_2	C	N_1	N_2	Fe_1	Fe_2	C	N_1	N_2	Fe_1	Fe_2
N/C>R_{NC}		+		+			+		+		+		+		
N/C<R_{NC}	+				+	+				+	+		+		

2.3 Organic and Inorganic Pools

There are two pools of detritus with different sinking rates but the same fixed elemental ratios. Detrital C/N/Fe ratios are the same as zooplankton, so zooplankton mortality or grazing of small zooplankton by large zooplankton produce no 'excess'. Phytoplankton mortality, and defecation by zooplankton grazing on phytoplankton, produces excess nutrient or excess C that needs to be recycled into the inorganic pool in a similar fashion as outlined above for the assimilated fraction of grazing on phytoplankton.

The conservation equations for detrital C are

$$\frac{dD_s}{dt} = m_1(C_{ps} + Z_s) + m_2(C_{ps}^2 + Z_S^2) - r_1 D_s T_g - w_s \frac{dD_s}{dz} \tag{17a}$$

$$\frac{dD_l}{dt} = m_1(C_{pl} + Z_L) + m_2(C_{pl}^2 + Z_L^2) - r_2 D_l T_g - w_l \frac{dD_l}{dz} \tag{17b}$$

where T_g is an Arrhenius function for temperature dependence of remineralization and w is the sinking speed. The conservation equations for inorganic C, N, and Fe are

$$\frac{dC_i}{dt} = (\zeta V^N - P_{phot}^C)C_p + R + C_{XS} + (r_1 D_s + r_2 D_l)T_g \tag{18a}$$

$$\frac{dN_i}{dt} = -\frac{V^N}{Q^N}N_p\left(\frac{L_{NO3}}{L_{NO3}+L_{NH4}}\right) + N_{ox} - N_{dentr}(1 - A_f) \tag{18b}$$

$$\frac{dN_a}{dt} = -\frac{V^N}{Q^N}N_p\left(\frac{L_{NH4}}{L_{NO3}+L_{NH4}}\right) + \frac{R}{R_{CN}} + N_{XS} + (r_1 D_s + r_2 D_l)R_{NC}T_g - N_{ox} + N_{dnf} - N_{dentr}A_f \tag{18c}$$

$$\frac{dFe}{dt} = \frac{V^{Fe}}{Q^{Fe}}Fe_p + \frac{R}{R_{CFe}} + Fe_{XS} + (r_1 D_s + r_2 D_l)R_{FeC}T_g \tag{18d}$$

where N_{ox} is microbial oxidation of ammonium to nitrate (nitrification), N_{dnf} and N_{dentr} are sources and sinks associated with dinitrogen fixation and denitrification, and A_f is the ammonium fraction of denitrification losses, associated with anaerobic ammonium oxidation ("anammox").

283 The oxygen equation is essentially the inverse of equation 18a, with additional terms for

284 oxidation and reduction of N, i.e.,

285 $\frac{dO_2}{dt} = -\frac{dC_i}{dt} + 2\frac{V^N}{Q^N}N_p(\frac{L_{NO3}}{L_{NO3}+L_{NH4}}) - 2N_{ox}$ (19)

286 Nitrification is given by

287 $N_{ox} = k_{NH4ox}N_a\frac{K_E}{K_E+E(z)}$ (20)

288 where $E(z)$ is the layer mean irradiance at depth z. Dinitrogen fixation is parameterized as an

289 external input of ammonium dependent on light, temperature and Fe availability, and inhibited

290 by high ambient concentrations of inorganic N,

291 $N_{dnf} = k_{dnf}T_{dnf}(1 - e^{-aE})(\frac{Fe}{K_{Fe}+Fe})(\frac{K_{NO3}}{K_{NO3}+N_i+N_a})$ (21)

292 where T_{dnf}=max(0, 1.962(T_f- 0.773)), i.e., a linear multiple of equation (1) that is 0 at T<20°C

293 and unity at T=30°C. The temperature, iron and light limitation terms are based on PISCES

294 (Aumont et al., 2015); the N-inhibition term is from CMOC (Zahariev et al., 2008) (CMOC

295 implicitly combines nitrate and ammonium into a single inorganic N pool).

296

297 Denitrification is parameterized as a fraction of total remineralization that increases as a linear

298 function of oxygen concentration for concentrations less than a threshold concentration O_{mxd}

299 $N_{frxn} = 1 - \frac{\min(O_2,O_{mxd})}{O_{mxd}}$ (22)

300 Remineralization is then divided among oxygen (1-N_{frxn}), nitrate (0.875N_{frxn}), and ammonium

301 (0.125N_{frxn}) assuming an average anammox contribution of 25% (Babbin et al., 2014). We use

302 this average ratio of anammox to classical denitrification to partition fixed N losses between

303   NO_3^- and NH_4^+; the DIC sink and organic matter source associated with anammox are small and

304   are neglected here.

305

306   **2.4 Calcification, Calcite Dissolution, and Alkalinity**

307

308   In CanOE, calcification is represented by a prognostic detrital calcite pool with its own sinking

309   rate (distinct from that of organic detritus), and calcite burial or dissolution in the sediments

310   depends on the saturation state (100% burial when $\Omega_C \geq 1$, 100% dissolution when $\Omega_C < 1$).

311   Calcification is represented by a detrital calcium carbonate ($CaCO_3$) state variable, but no

312   explicit calcifier groups. Detrital $CaCO_3$ sinks in the same fashion as detrital particulate organic

313   carbon (POC), with a sinking rate independent of those for large and small organic detritus.

314   Calcite production is represented as a fixed fraction of detritus production from small

315   phytoplankton and small zooplankton mortality:

316   $$\frac{dCa}{dt} = m_1\big(C_{ps} + Z_s\big)P_{Ca} + m_2\big(C_{ps}^2 + Z_s^2\big)P_{Ca} - k_{Ca}Ca - w_{Ca}\frac{dCa}{dz} \qquad (23)$$

317   Calcite dissolution occurs throughout the water column as a first order process (i.e., no

318   dependence on temperature or saturation state). Approximately 80% of calcite produced is

319   exported from the euphotic zone. In CanESM5-CanOE, burial in the sediments is represented as

320   a simple 'on/off' switch dependent on the calcite saturation state (zero when $\Omega_C < 1$ and 1 when

321   $\Omega_C \geq 1$). In CanESM5, calcification is parameterized by a temperature dependent "rain ratio"

322   (Zahariev et al., 2008) and 100% burial of calcite that reaches the seafloor is assumed. Calcite

323   burial in both models is balanced by an equivalent source of DIC and alkalinity at the ocean

324   surface (in the same vertical column) as a crude parameterization of fluvial sources.

325

For each mole of calcite production, two moles of alkalinity equivalent are lost from the

dissolved phase; the reverse occurs during calcite dissolution. There are additional sources and

sinks for alkalinity associated with phytoplankton nutrient (NH_4^+, NO_3^-) uptake, organic matter

remineralization, nitrification, denitrification and dinitrogen fixation (Wolf-Gladrow et al., 2007,

see Supplementary Table S2). The anammox reaction does not in itself contribute to alkalinity

(Jetten at al., 2001), but there is a sink associated with ammonium oxidation to nitrite (the model

does not distinguish between nitrite and nitrate). Autotrophic production of organic matter by

anammox bacteria is a net source of alkalinity (Strous et al., 1998), but this source is extremely

small (~0.03 mol/molN) and is neglected here. Globally, the sources and sinks of alkalinity from

the N cycle offset each other such that there is no net gain or loss as long as the global fixed N

pool is conserved (see below Sect. 2.5). If dinitrogen fixation and denitrification are allowed to

vary freely, there will generally be a net gain or loss of fixed N and, therefore, of alkalinity.

338

2.5 External Nutrient Sources and Sinks

340

External sources and sinks consist of river inputs, aeolian deposition, biological N_2 fixation,

denitrification, mobilization of Fe from reducing sediments, loss of Fe to scavenging, and burial

of calcium carbonate in the sediments. There is no burial of organic matter; organic matter

reaching the seafloor is instantaneously remineralized. Aeolian deposition of Fe is calculated

from a climatology of mineral dust deposition generated from offline (atmosphere-only)

simulations with CanAM4 (von Salzen et al., 2013), with an Fe mass fraction of 5% and a

fractional solubility of 1.4% in the surface layer. Subsurface dissolution is parameterized based

348   on PISCESv2 (Aumont et al., 2015); the total dissolution is 6.35%, with 22% of soluble Fe input

349   into the first vertical layer (see Supplementary material). Iron from reducing sediments is also

350   based on PISCES, with a constant areal flux of 1000 nmol m^{-2} d^{-1} in the first model level,

351   declining exponentially with increasing seafloor depth (i.e., assuming that shelf sediments are the

352   strongest source and the sediments become progressively more oxygenated with increasing

353   seafloor depth) with an e-folding length scale of about 600 m. Scavenging of dissolved iron is

354   first-order with a high rate (2.5 d^{-1}) for concentrations in excess of 0.6 nM (Johnson et al., 1997).

355   For concentrations below this threshold, the rate is much lower (0.001 d^{-1}) and is weighted by the

356   concentration of organic detritus (Christian et al., 2002b), i.e.,

357    $$\frac{dFe}{dt} = -FeS_{Fe1} min\{(D_S + D_L)P_{Fe}, 1\} \qquad (24)$$

358   where Fe is the dissolved iron concentration, D_S and D_L are the small and large detritus

359   concentrations, S_{Fe1} is the first-order scavenging rate in surface waters with abundant

360   particulates, and P_{Fe} is an empirical parameter to determine the dependence on particle

361   concentration (Table 1). The basis for this parameterization is that the rate of scavenging must

362   depend not only on the concentration of iron but on the concentration of particles available for it

363   to precipitate onto, and assumes that detrital POC is strongly positively correlated with total

364   particulate matter. Scavenging is treated as irreversible, i.e., scavenged Fe is not tracked and

365   does not reenter the dissolved phase.

366

367   N_2 fixation and denitrification vary independently in CanOE, so the global total N pool can

368   change. Conservation is imposed by adjusting the global total N pool according to the difference

369   between the gain from N_2 fixation and the loss to denitrification. A slight adjustment is applied

370   to the nitrate concentration at every grid point, while preserving the overall spatial structure of

371 the nitrate field. Adjustments are multiplicative rather than additive to avoid producing negative

372 concentrations. This adjustment does not maintain (to machine precision) a constant global N

373 inventory but is intended to minimize long term drift, keeping it much smaller than the free

374 surface error (see below). This adjustment is applied every 10 days and has a magnitude of

375 approximately 7×10^{-8} of the total N.

376

377 When the total fixed N adjustment is applied, one mole of alkalinity is added (removed) per mole

378 of N removed (added), to account for the alkalinity sources associated with N_2 fixation (creation

379 of new NH_4^+) and denitrification (removal of NO_3^-) (Wolf-Gladrow et al., 2007, see

380 Supplementary Table S2). As there is a 2 mol/molN sink associated with nitrification, this

381 formulation is globally conservative. As noted above, in CanOE $CaCO_3$ can dissolve or be buried

382 in the sediments depending on the calcite saturation state. DIC and alkalinity lost to burial are

383 reintroduced at the ocean surface, at the same grid point as burial occurs, providing a crude

384 parameterization of river inputs so that global conservation is maintained (fresh water runoff

385 contains no DIC or alkalinity). However, the OPA free surface formulation is inherently

386 imperfect with regard to tracer conservation. Drift in total ocean alkalinity and nitrogen over

387 time is on the order of 0.01% and 0.03% per thousand years, respectively.

388

389 **2.6 Ancillary data**

390

391 For first-order model validation we have relied largely on global gridded data products rather

392 than individual profile data. Global gridded data from World Ocean Atlas 2018 (WOA2018)

393 (Locarnini et al., 2018; Zweng et al., 2018; Garcia et al., 2018a; 2018b) were used for

394   temperature, salinity, and oxygen and nitrate concentration. DIC and alkalinity were taken from

395   the GLODAPv2.2016b gridded data product (Key et al., 2015; Lauvset et al., 2016). Offline

396   carbon chemistry calculations were done following the Best Practices Guide (Dickson et al.,

397   2007) and the OMIP-BGC protocols (Orr et al., 2017), and are identical to those used in the

398   models except that constant reference concentrations were used for phosphate (1 µM) and

399   silicate (10 µM).

400

401   There is no global gridded data product for Fe, but we have made use of the GEOTRACES

402   Intermediate Data Product 2017 (Schlitzer et al., 2018), and the data compilations from MBARI

403   (Johnson et al., 1997; 2003) and PICES Working Group 22 (Takeda et al., 2013). The latter two

404   are concentrated in the Pacific, while GEOTRACES is more global. The combined data sets

405   provide more than 10000 bottle samples from more than 1000 different locations (Supplementary

406   Figure S10a) (excluding some surface transect data that involve frequent sampling of closely

407   spaced locations along the ship track). More detail about model comparison to these data

408   compilations and the list of original references are given in the Supplementary information.

409

410   Satellite ocean colour estimates of surface chlorophyll were taken from the combined

411   SeaWiFS/MODIS climatology described by Tesdal et al. (2016). Climatological satellite POC

412   was downloaded from the NASA ocean colour web site and is based on the algorithm of

413   Stramski et al. (2008) using MODIS-Aqua data. This climatology differs slightly from the

414   chlorophyll one in terms of years included and sensors utilized, but as only climatological

415   concentrations are considered and each climatology covers ~15 years, these differences will have

416   negligible effect on the results presented. Satellite chlorophyll concentrations greater than 1 mg

417 m^{-3} were excluded as these are mostly associated with coastal regions not resolved by coarse-

418 resolution global ocean models.

419

420 CMIP6 model data were regridded by distance-weighted averaging using the Climate Data

421 Operators (https://code.mpimet.mpg.de/projects/cdo/) to a common grid (2x2°, 33 levels) to

422 facilitate ensemble averaging. The vertical levels used are those used in GLODAP and in earlier

423 (through 2009) versions of the World Ocean Atlas (e.g., Locarnini et al., 2010). For large scale

424 tracer distributions, using a 1° or 2° grid makes little difference (for example, the spatial pattern

425 correlation between CanESM5 and observed oxygen concentration at specific depths on a 1° or

426 2° grid differs by an average of 0.0011). The years 1986-2005 of the Historical experiment were

427 averaged into climatologies or annual means, for meaningful comparison with observation-based

428 data products. The CMIP6 Historical experiment runs from 1850-2014 with atmospheric CO_2

429 concentration (and other atmospheric forcings) based on historical observed values. A single

430 realization was used in each case (see Table S3); 20 year averages are used to minimize the

431 effect of internal variability (e.g., Arguez and Vose, 2011, see Table S4). Where time series are

432 shown, 5-year means are used.

433

434 Sampling among CMIP6 models was somewhat opportunistic, and the exact suite of models

435 varies among the analyses presented. When we conducted a search for a particular data field, we

436 included in the search parameters all models that published that field, and repeated the search at

437 least once for models that were unavailable the first time the search was executed. In some cases,

438 model ensemble means excluded all but one model from a particular 'family' (e.g., there are

439 three different MPI-ESM models for which ocean biogeochemistry fields were published), as the

440   solutions were found to be similar and would bias the ensemble mean towards their particular

441   climate. The models used are ACCESS-ESM1-5, CESM2, CESM2-WACCM, CNRM-ESM2-1,

442   GFDL-CM4, GFDL-ESM4, IPSL-CM6A-LR, MIROC-ES2L, MPI-ESM-1-2-HAM, MPI-

443   ESM1-2-LR, MPI-ESM1-2-HR, MRI-ESM2-0, NorESM2-LM, NorESM2-MM, and UKESM1-

444   0-LL. Details of which variables and realizations are used for which models are given in

445   Supplementary Table S3.

446

447   **3. Results**

448

449   We first describe the large-scale distribution of oxygen, DIC, alkalinity, and the saturation state

450   with respect to $CaCO_3$ that derives from these large-scale tracer distributions. Tracer

451   distributions result partly from ocean circulation and partly from biogeochemical processes. An

452   overall evaluation of the ocean circulation model is given in Swart et al. (2019a). Analyzing

453   CanESM5 and CanESM5-CanOE (with identical circulation) as well as CanESM2 where

454   possible (same biogeochemistry as CanESM5 but different circulation) allows us to separate the

455   effects of physical circulation and biogeochemistry on evolving model skill with respect to large-

456   scale tracer distributions. In subsequent sections we address the main areas where CanESM5 and

457   CanESM5-CanOE differ, such as the interaction of the iron and nitrogen cycles and plankton

458   community structure. Finally, we present some temporal trends over the course of the historical

459   experiment (1850-2014).

460
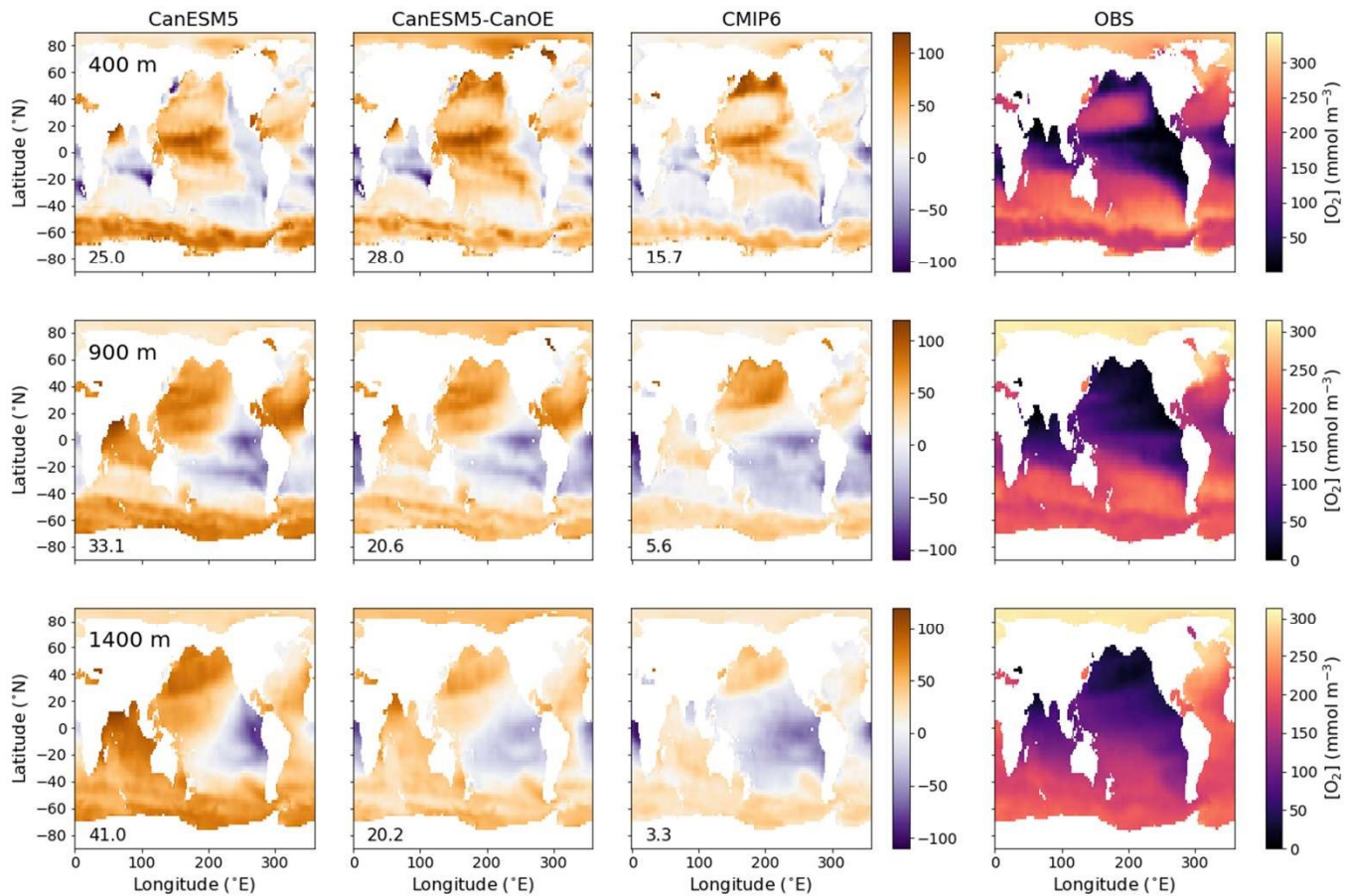
Figure 2 - Global distribution of oxygen (O_2) concentration in mmol m^{-3} at 400, 900, and 1400 m (rows). Observations (WOA2018) are in the right hand column; other columns show the difference from the observations of CanESM5-CanOE, CanESM5, and the mean for other CMIP6 models. Note different colour scales for different rows. Numbers at lower left are the mean model bias. Model concentrations are shown in Supplementary Figure S3.

3.1 Distribution of oxygen

The spatial distribution of oxygen concentration ($[O_2]$) at selected intermediate depths (400, 900, and 1400 m) is shown in Figure 2 for gridded data from WOA2018 and differences from that observational data product for CanESM5, CanESM5-CanOE, a model ensemble mean (MEM) of CMIP6 models (excluding CanESM5 and CanESM5-CanOE). The depths were chosen to span the depth range where low oxygen concentrations exist; these low-oxygen environments are of substantial scientific and societal interest and are sensitive to model formulation. The major features are consistent across the models. Both CanESM models as well as the MEM show elevated oxygen concentrations relative to observations, particularly in the North Pacific, the North Atlantic and the Southern Ocean. In the Indian Ocean, both CanESM models show high oxygen concentrations in the Arabian Sea and deeper layers of the Bay of Bengal relative to observations and the MEM; these biases are somewhat smaller in CanESM5-CanOE than in CanESM5 (Figure 2).

The ocean's oxygen minimum zones (OMZs) are mostly located in the eastern Pacific Ocean, the northern North Pacific, and the northern Indian Ocean; the spatial pattern changes with increasing depth (Figure 2), but the OMZs are mostly located between 200 and 2000 m depth. Biases in the EBC regions are depth and model specific. CanESM5 shows particularly strong oxygen depletion at 1400 m in the eastern tropical Pacific. In the southeastern Atlantic, models tend to be biased low at the shallower depths, and show somewhat more variation at greater depths (Figure 2). Overall, $[O_2]$ biases tend to be positive over large areas of ocean with the exception of some EBC regions, implying that models exaggerate the extent to which
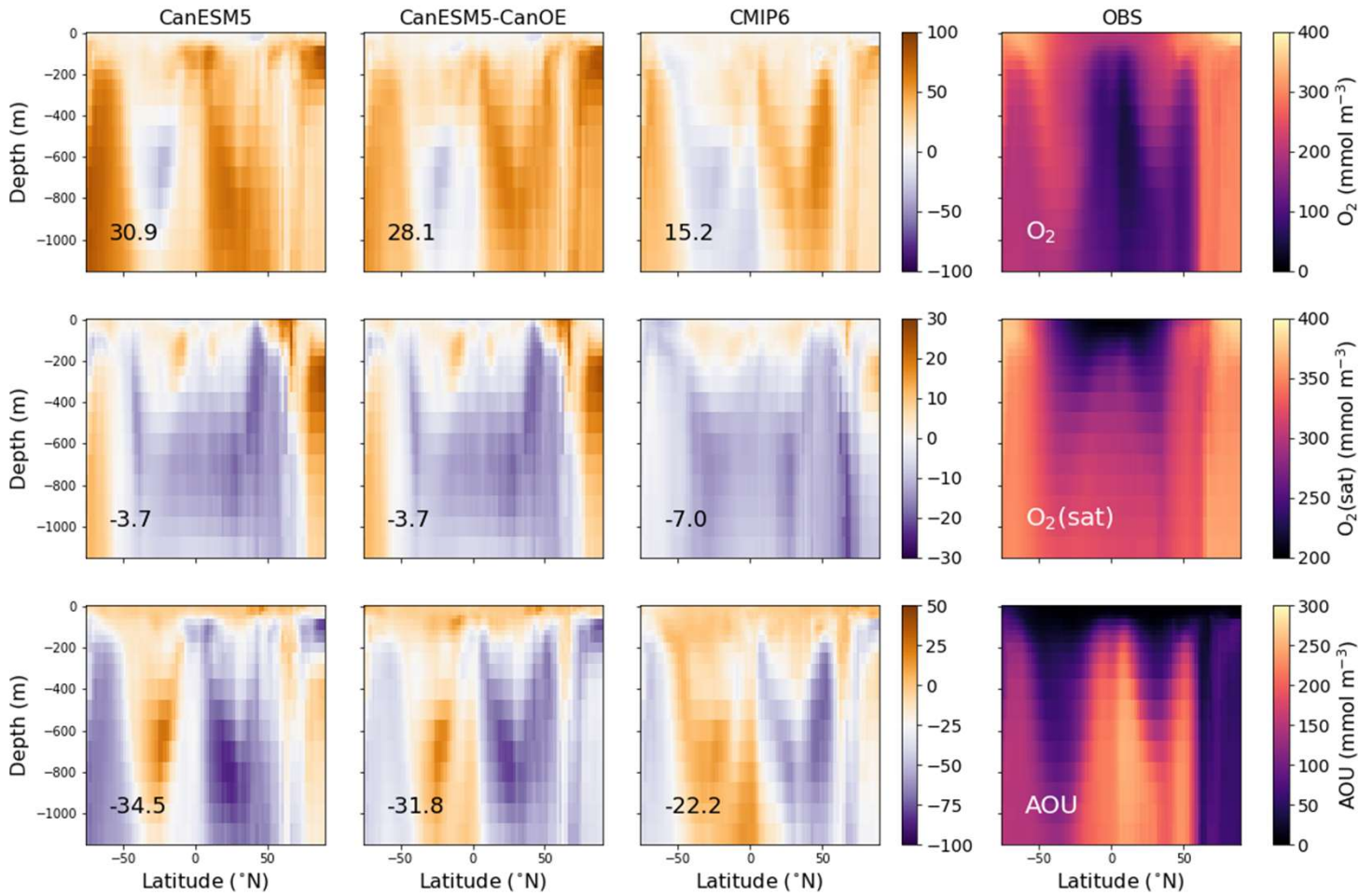
Figure 3 - Latitude-depth distribution (surface to 1750 m) of zonal mean oxygen concentration (O_2), oxygen concentration at saturation (O_2(sat)), and apparent oxygen utilization (AOU) in mmol m^{-3}. Observations (WOA2018) are in the right hand column; other columns show the difference from the observations of CanESM5-CanOE, CanESM5, and the mean for other CMIP6 models. Note different colour scales for different rows. Numbers at lower left are the mean model bias. Model concentrations are shown in Supplementary Figure S3.

486   remineralization is concentrated in these regions. An alternate version of Figure 2 that shows the

487   modelled concentrations is given in Supplementary Figure S2.

488

489   The zonal mean oxygen concentration, saturation concentration, and apparent oxygen utilization

490   (AOU) are shown in Figure 3 for the same four cases. Again, the models generally show a

491   positive bias in [O_2], particularly in high-latitude deep waters. The major ocean circulation

492   features are reproduced fairly well in all cases (e.g., weaker ventilation of low-latitude

493   subsurface waters, greater vertical extent of well-ventilated surface waters in the subtropics). The

494   saturation concentration (a function of temperature and salinity) generally shows relatively little

495   bias, implying that the bias in [O_2] arises mainly from remineralization and/or ventilation. AOU

496   is lower than observed over much of the subsurface ocean. CanESM5 and CanESM5-CanOE

497   show a high bias over much of the Northern Hemisphere that reflects the high concentrations in

498   the North Pacific and North Atlantic (Figure 2). The overall trend of bias with latitude in

499   CanESM5 and CanESM5-CanOE is generally similar to the MEM, but the biases are larger. The

500   bias in CanESM5 is generally slightly larger than in CanESM5-CanOE, except in the Arctic

501   Ocean. Again, Supplementary Figure S2 includes a version of this plot that shows the modelled

502   concentration fields.

503

504   The skill of each model with respect to the distribution of O_2 at different depths is represented by

505   Taylor diagrams (Taylor, 2001) in Figure 4. These diagrams allow us to assess how well the

506   model reproduces the spatial distribution at a range of depths, because different physical and

507   biogeochemical processes determine the distribution in different depth ranges. All of the CMIP6

508   models that were shown as an ensemble mean in Figures 2 and 3 are shown individually. The
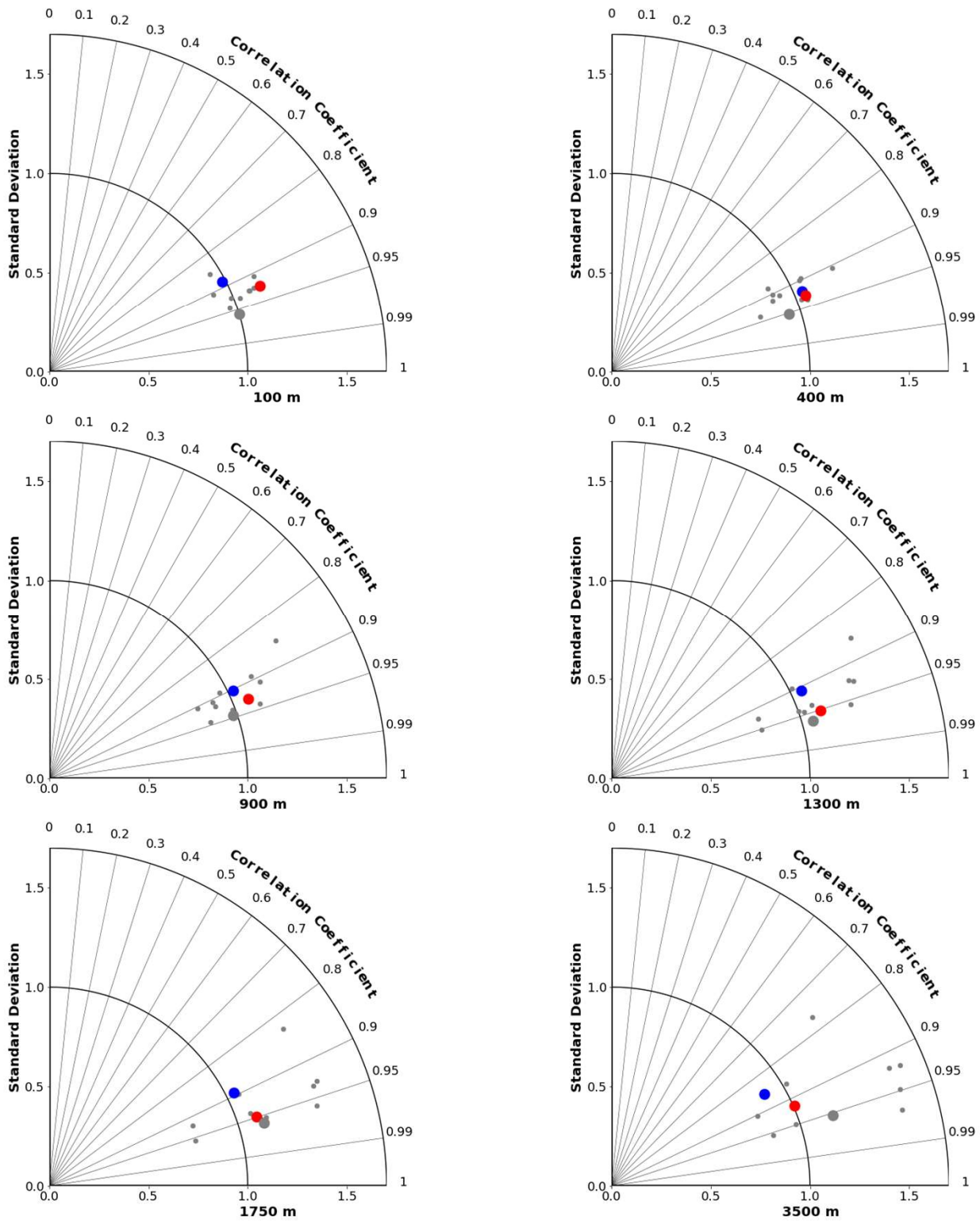
Figure 4 - Taylor diagrams (Taylor, 2001) comparing modelled and observed distributions of oxygen at specific depths from 100 to 3500 m. Angle from the vertical indicates spatial pattern correlation. Distance from the origin indicates ratio of standard deviation in modelled vs. observed (WOA2018) fields. Red dots represent CanESM5-CanOE, blue dots CanESM5, small grey dots other CMIP6 models, and large grey dots the model ensemble mean for all CMIP6 models except CanESM5 and CanESM5-CanOE.
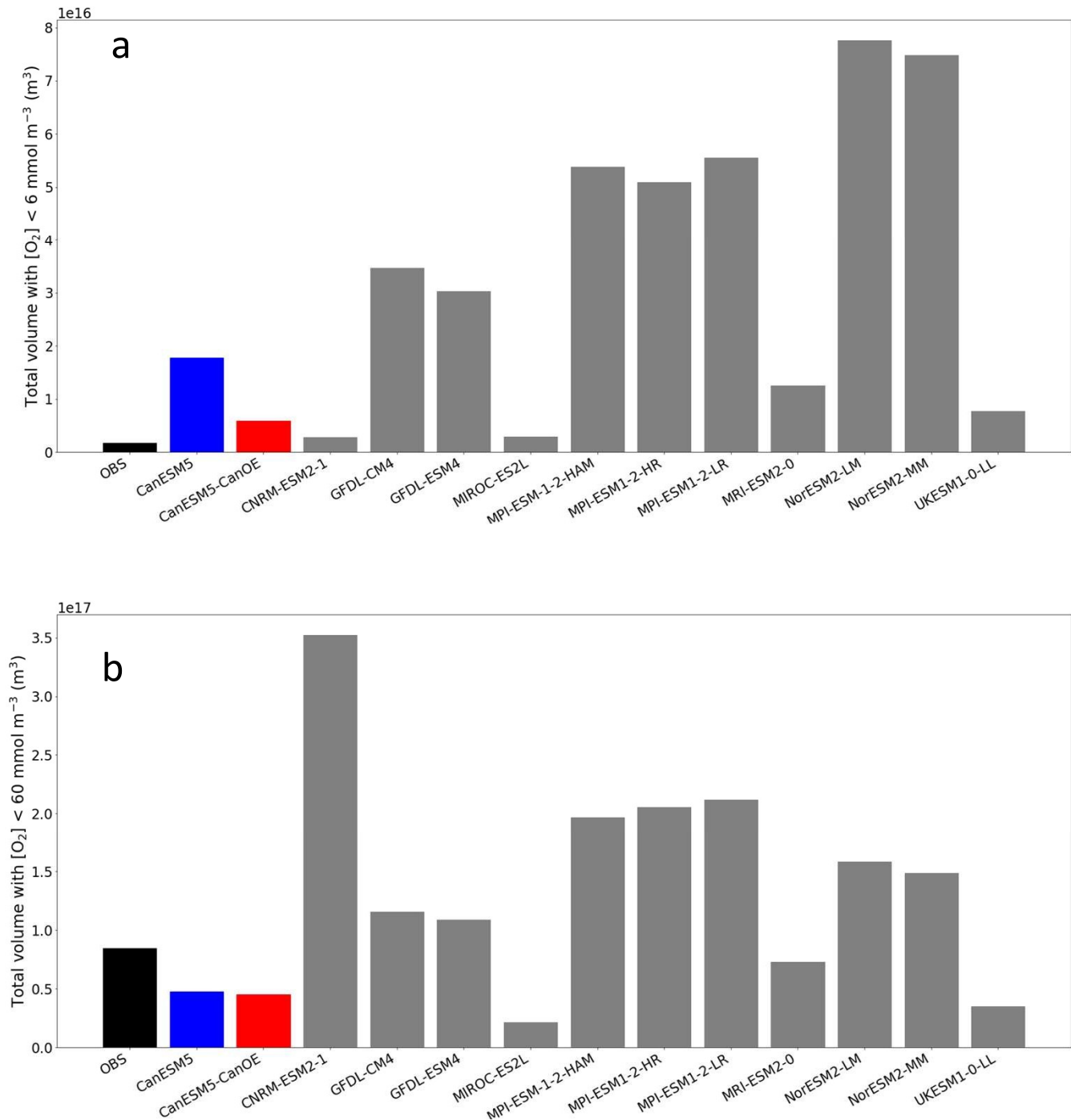
Figure 5 - Total volume of ocean with oxygen (O_2) concentration less than (a) 6 mmol m^{-3} (mean for last 30 years of the historical experiment) and (b) 60 mmol m^{-3}. Observation are from WOA2018.

511   large blue dots represent CanESM5, red CanESM5-CanOE, and grey the MEM; the smaller grey

512   dots represent the individual models. CanESM5-CanOE shows slightly higher pattern correlation

513   than CanESM5 at all depths. Both models compare favourably with the full suite of CMIP6

514   models, with r>0.85 for CanESM5 and r>0.9 for CanESM5-CanOE at all depths examined, and a

515   normalized standard deviation within ±25% of unity.

516

517   The total volume of ocean with $[O_2]$ less than 6 mmol m^{-3} (the threshold for denitrification

518   (Devol, 2008)) and 60 mmol m^{-3} (a commonly used index of hypoxia) is shown in Figure 5. The

519   total volume is highly variable among models (note, however, that there are several clusters of

520   related models with quite similar totals). CanESM5 and CanESM5-CanOE have among the

521   lowest total volumes (i.e., the interior ocean is relatively well ventilated) and are among the

522   nearest to the observed total. For $[O_2]$ <60 mmol m^{-3} the bias is, nonetheless, quite large (i.e., the

523   observed volume is underestimated by almost 50% in both models). The volume of water with

524    $[O_2]$ below the denitrification threshold is overestimated in both CanESM5 and CanESM5-

525   CanOE; CanESM5-CanOE has a much smaller total that is closer to the observed value. The bias

526   in the spatial pattern of hypoxia (not shown) is generally similar to the bias in dissolved oxygen

527   distribution (Figure 2). The low-oxygen regions are generally more concentrated in the eastern

528   tropical Pacific in the models than in observations, and the low-oxygen region in the northwest

529   Pacific is not well reproduced in CanESM models.

530

531   **3.2 Distribution of DIC, alkalinity, and CaCO$_3$ saturation**

532

533   The spatial distribution of aragonite saturation state (Ω_A) at selected depths is shown in Figure 6.
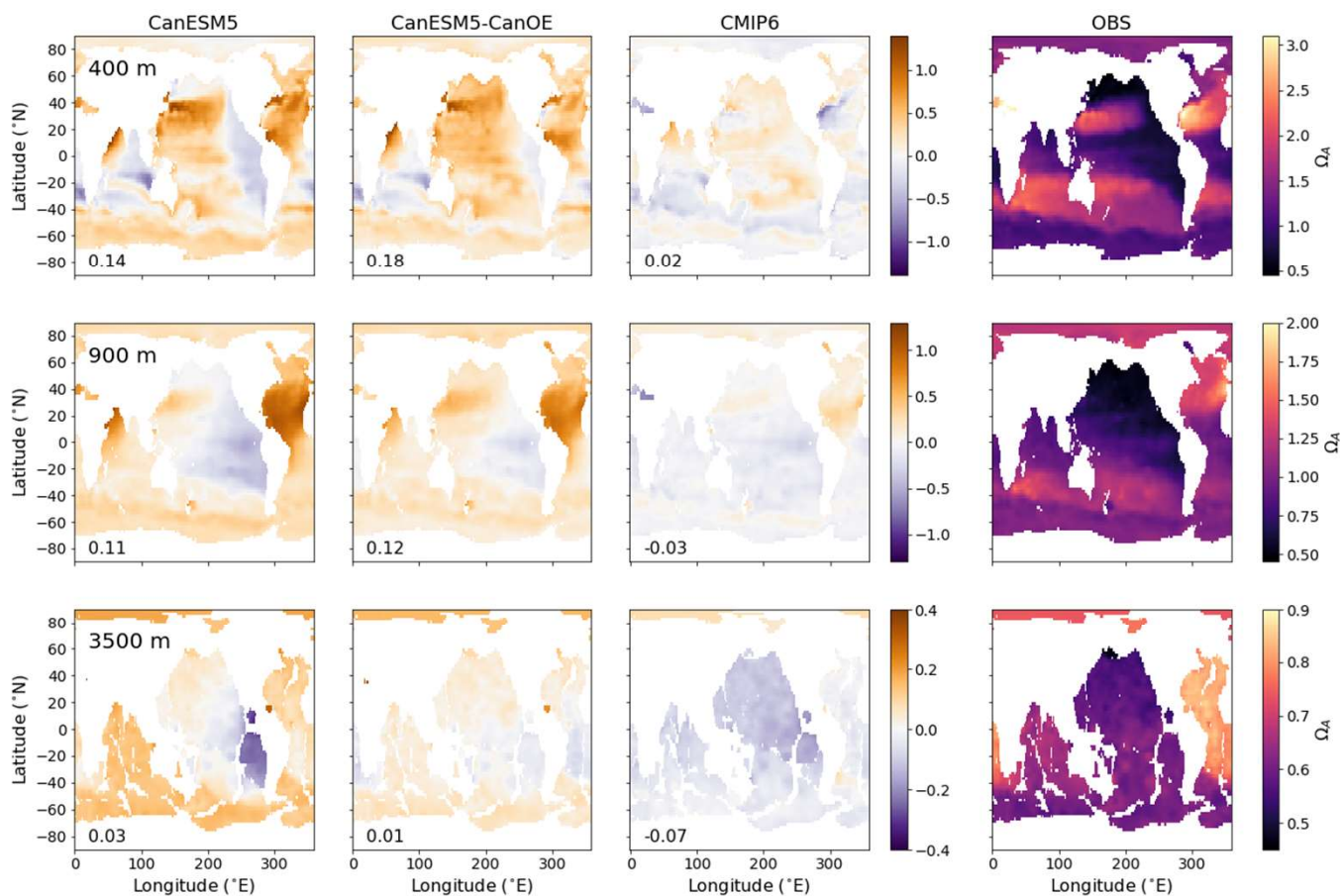
Figure 6 - Global distribution of aragonite saturation (Ω_A) at 400, 900, and 3500 m for CanESM5-CanOE, CanESM5, the mean for other CMIP6 models, and observations (GLODAPv2 + WOA2018). Note different colour scales for different depths. Numbers at lower left are the mean model bias. Difference from the observation-based fields are shown in Supplementary Figure S3.

535   The first two depths are the same as in Figure 2, but a much greater depth is also included, as the

536   length scale for $CaCO_3$ dissolution is greater than for organic matter remineralization. In this

537   case the observations are a combination of GLODAPv2 (Key et al., 2015; Lauvset et al., 2016)

538   for DIC and alkalinity, and WOA2018 for temperature and salinity. CanESM5 and CanESM5-

539   CanOE show an overall high saturation bias at the shallower depths, particularly in the North

540   Atlantic, with a low bias found mainly in the eastern Pacific. The low saturation bias in the

541   eastern tropical Pacific is substantially reduced in CanESM5-CanOE compared to CanESM5. On

542   the other hand CanESM5 generally does better than CanESM5-CanOE, or the MEM, at

543   reproducing the low saturation states in the northwestern Pacific and the Bering Sea. Both

544   CanESM models show a high saturation state bias in the North Atlantic and the well-ventilated

545   regions of the north Pacific subtropical gyre; these biases are slightly smaller in CanESM5-

546   CanOE. Maps of the calcite and aragonite saturation horizon (Ω=1) depth are shown in

547   Supplementary Figure S3; these generally confirm the same biases noted in Figure 6.

548

549   Zonal mean distributions of aragonite saturation state (Ω_A), calcite saturation state (Ω_C), and

550   carbonate ion concentration ($[CO_3^{--}]$) and the differences of the models from the observations are

551   shown in Figure 7 (Supplementary Figure S2 includes versions of Figures 6 and 7 that show the

552   modelled fields). The models generally compare well with the observations in the representation

553   of the latitude/depth distribution of high and low saturation waters. CanESM5 has a high

554   saturation bias in low-latitude surface waters that is somewhat reduced in CanESM5-CanOE.

555   Both CanESM5 models show a high saturation bias in Northern Hemisphere intermediate (e.g.,

556   200-1000 m) depth waters that is larger than in the MEM. This is primarily a result of low Ω in

557   the North Atlantic Ocean (Figure 6).
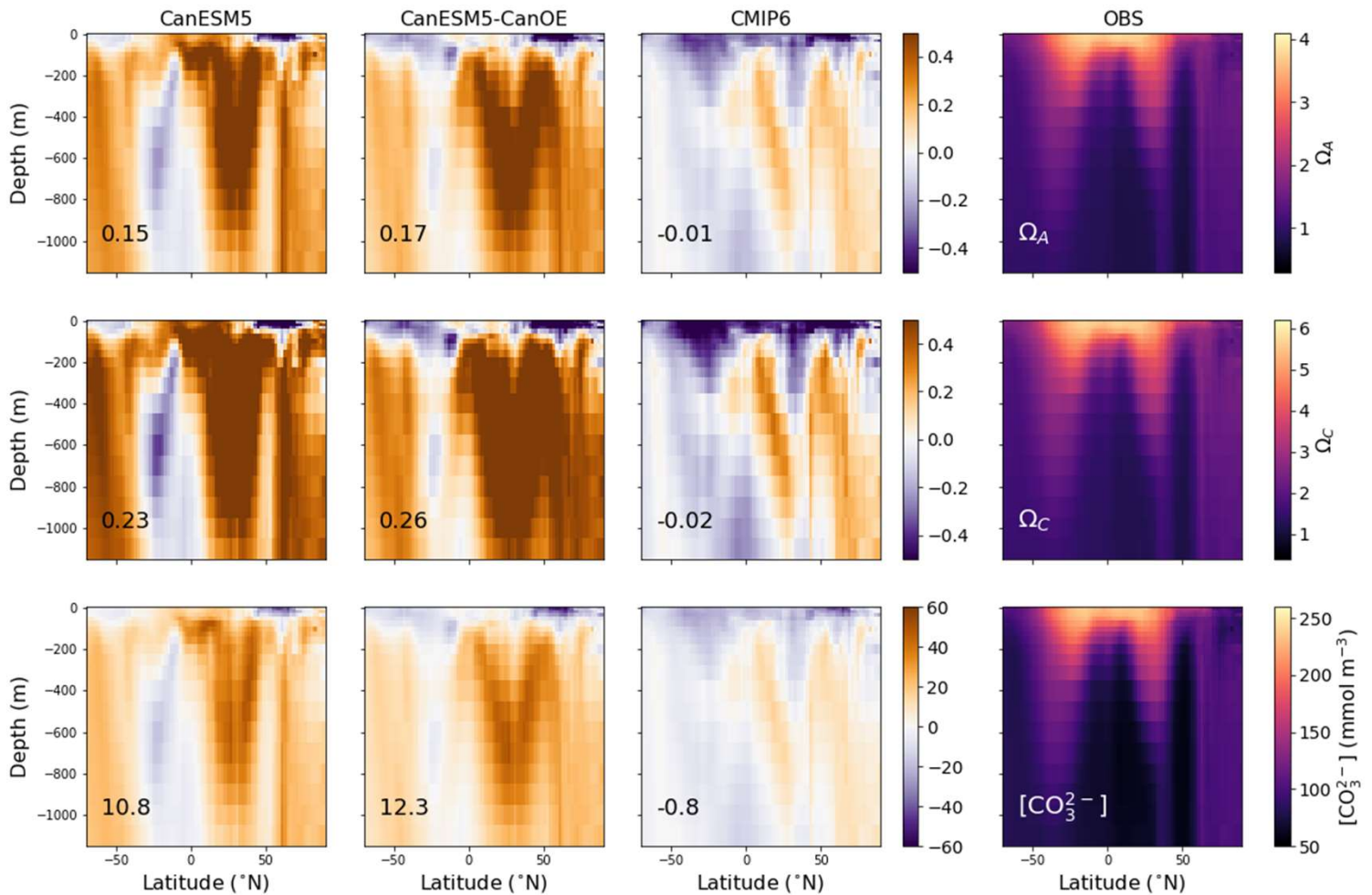
Figure 7 - Latitude-depth distribution of zonal mean (surface to 1150 m) aragonite saturation state (Ω_A), calcite saturation state (Ω_C), and carbonate ion concentration ([CO3--]) in mmol m^{-3} for CanESM5-CanOE, CanESM5, the mean for other CMIP6 models, and observations (GLODAPv2 + WOA2018). Numbers at lower left are the mean model bias. Difference from the observation-based fields are shown in Supplementary Figure S3.
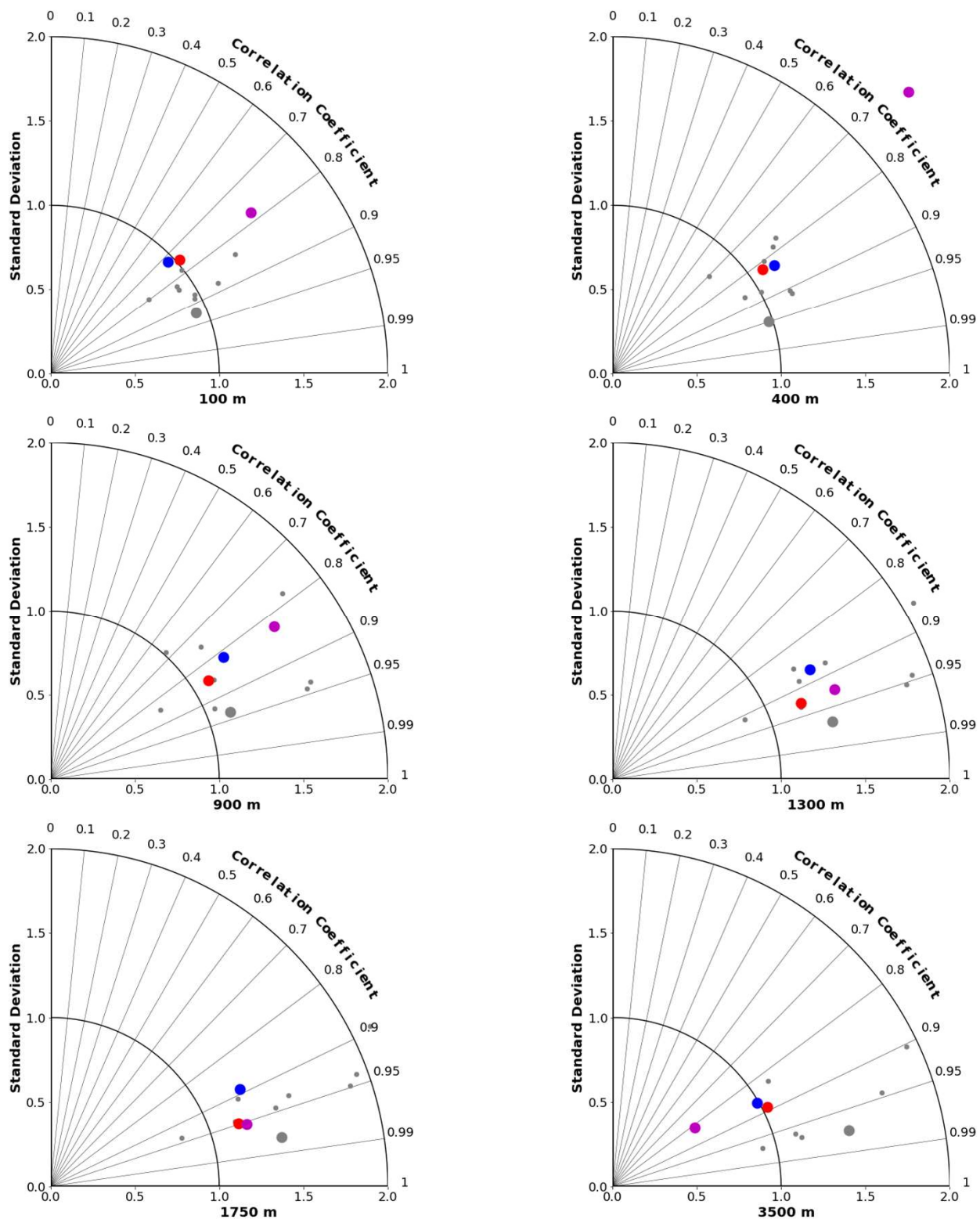
Figure 8 - Taylor diagrams comparing modelled and observed distributions of DIC at specific depths from 100 to 3500 m. Observations are from GLODAPv2 (Key et al., 2015; Lauvset et al., 2016). Red dots represent CanESM5-CanOE, blue dots CanESM5, magenta dots CanESM2, small grey dots other CMIP6 models, and large grey dots the model ensemble mean for all CMIP6 models except CanESM5 and CanESM5-CanOE.
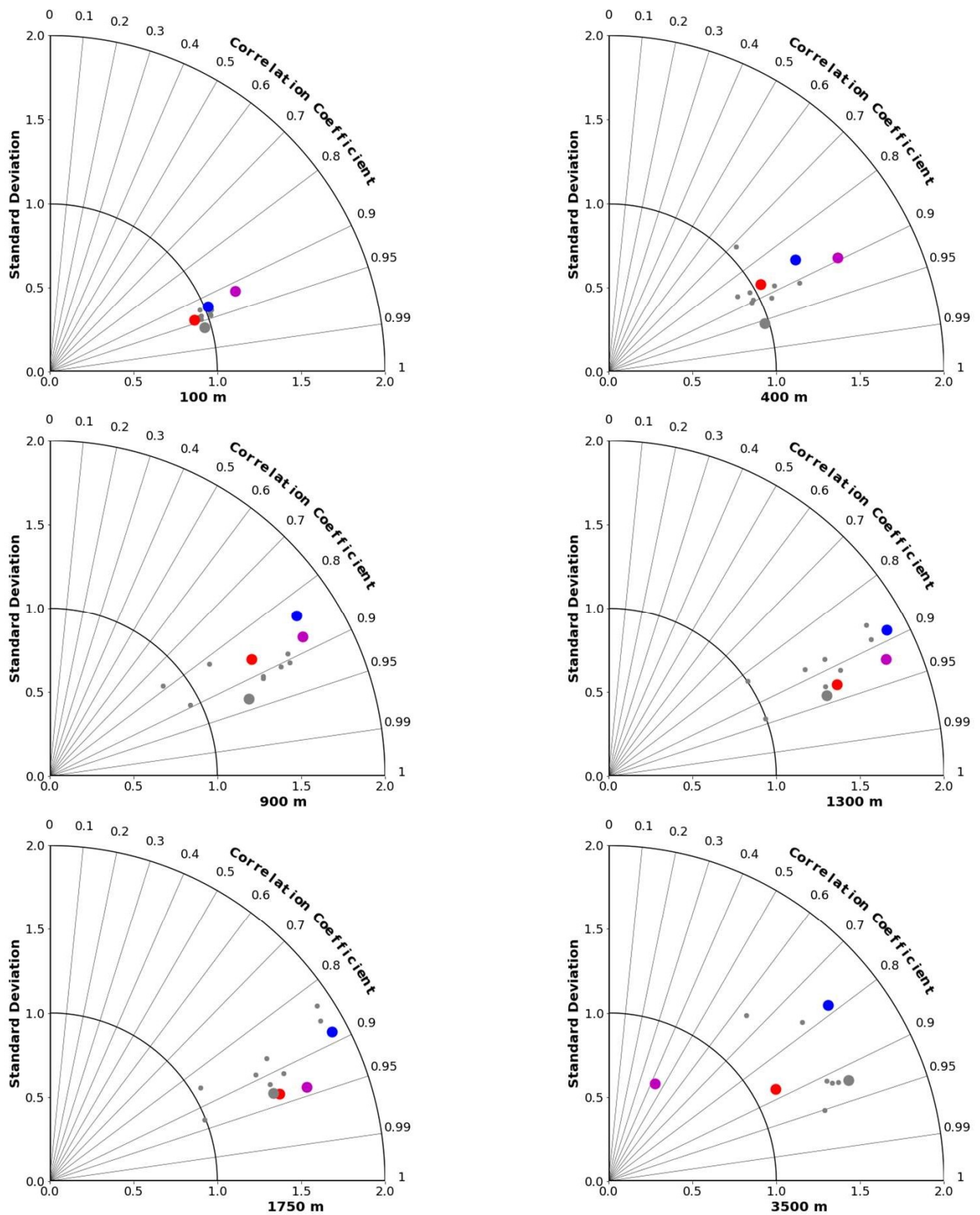
Figure 9 - Taylor diagrams comparing modelled and observed (GLODAPv2 + WOA2018) distributions of Ω_A at specific depths from 100 to 3500 m. Symbol colours as in Figure 8.

561 Taylor diagrams for a range of depths are shown for DIC in Figure 8 and for Ω_A in Figure 9 (for

562 alkalinity, see Supplementary Figure S4). As expected, the MEM generally compares favourably

563 with the individual models (e.g., Lambert and Boer, 2001). CanESM5 and CanESM5-CanOE

564 compare favourably with the full suite of CMIP6 models. CanESM5-CanOE shows a gain in

565 skill relative to CanESM5, and both show improvement relative to CanESM2. At 400 m,

566 CanESM2 stands out as having extremely high variance, which is mostly due to extremely high

567 DIC concentrations occurring over a limited area in the eastern equatorial Pacific (not shown).

568 This bias is present in CanESM5 and in CMIP6 models generally (Figure 6) but involves much

569 lower concentrations spread over a larger area.

570

571 **3.3 N and Fe cycles**

572

573 An important difference between CanESM5 and CanESM5-CanOE is the inclusion of a

574 prognostic Fe cycle. The CMOC iron mask (Zahariev et al., 2008) was a pragmatic solution in

575 the face of resource limitations but is inherently compromised as it can not evolve with a

576 changing climate. The first order test of a model with prognostic, interacting Fe and N cycles is

577 whether it can reproduce the distribution of HNLC regions and the approximate surface

578 macronutrient concentrations within these. CanESM5-CanOE succeeded by this standard,

579 although the surface nitrate concentrations are biased low in the subarctic Pacific and equatorial

580 Pacific and high in the Southern Ocean and in the global mean (Figure 10).

581

582 The seasonal cycle of the zonal mean surface nitrate concentration for a selection of CMIP6

583 models is shown in Figure 11. CanESM5, CanESM5-CanOE, and CNRM-ESM2-1 reproduce the
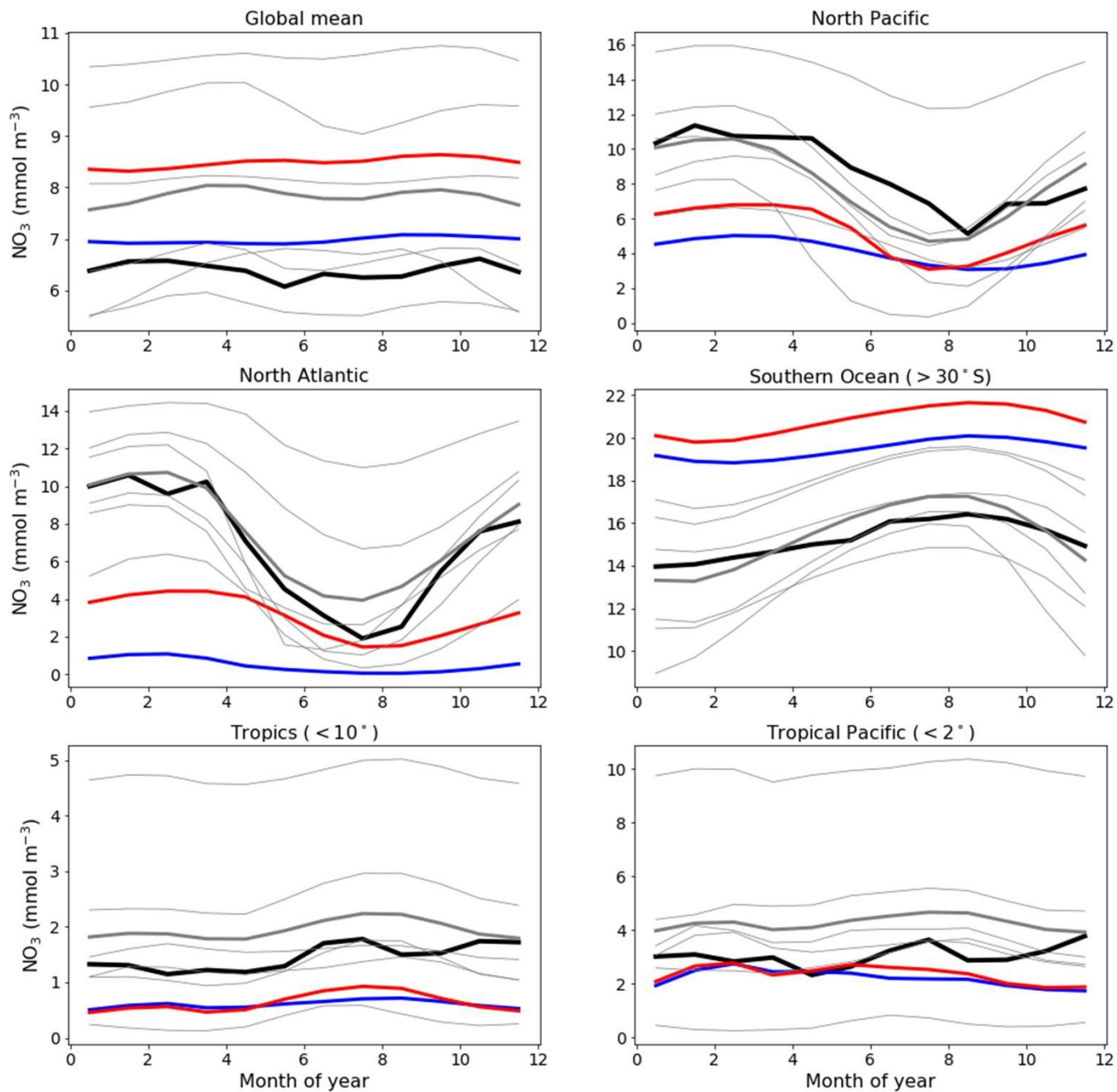
Figure 10 - Climatological seasonal cycle of surface nitrate concentration averaged for selected ocean regions. Thick red line represents CanESM5-CanOE, thick blue line CanESM5, thick black line observations (WOA2018), thin grey lines individual CMIP6 models, and thick grey line the model ensemble mean (excluding CanESM5 and CanESM5-CanOE). Regional boundaries are given in Supplementary Table S5 and Supplementary Figure S5.
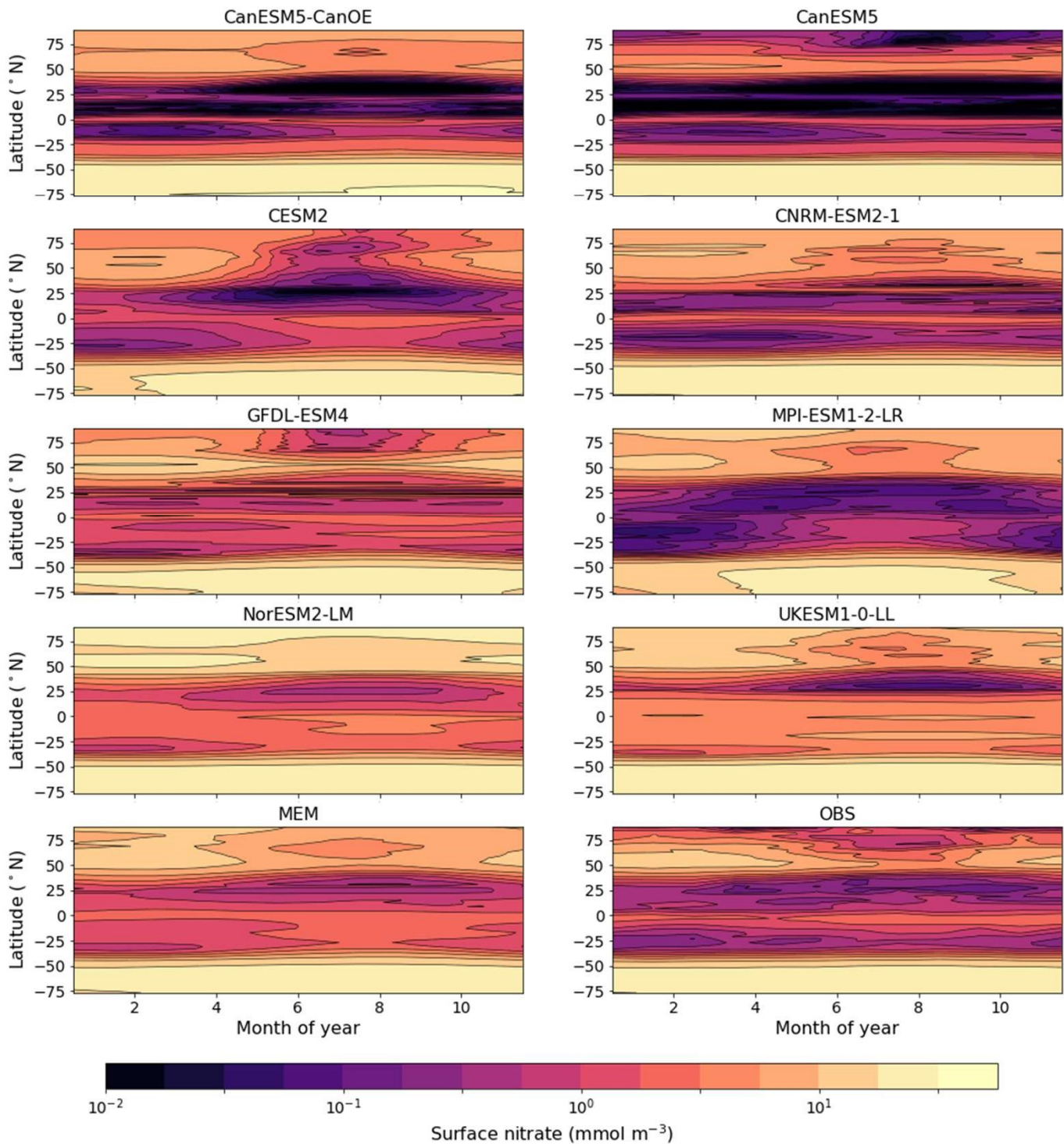
Figure 11 - Climatological seasonal cycle of zonal mean surface nitrate concentration for a selection of CMIP6 models, a model ensemble mean (MEM) excluding CanESM5 and CanESM5-CanOE, and an observation-based data product (WOA2018). An alternate version showing only latitudes <20° is given in Supplementary Figure S6.

586 equatorial enrichment and the low concentrations in the tropical-subtropical latitudes fairly well.

587 Some models either have very weak equatorial enrichment (MPI-ESM1-2-LR) or too high a

588 concentration in the off-equatorial regions (UKESM1-0-LL, NorESM2-LM). UKESM1-0-LL

589 has very high concentrations throughout the low-latitude Pacific, which biases the ensemble

590 mean (Figure 11). Supplementary Figure S6 shows the same data as Figure 11 but for a more

591 limited latitude range to better illustrate model behaviour in the tropics. CanESM5, CanESM5-

592 CanOE, and CNRM-ESM2-1 reproduce the seasonal cycle of tropical upwelling (e.g., Philander

593 and Chao, 1991), with highest concentrations in summer.

594

595 The surface distribution of dissolved iron (dFe) in various CMIP6 models is shown in Figure 12.

596 For Fe there is no observation-based global climatology with which to compare the model

597 solutions (some comparisons to available profile data are shown in Supplementary Figures S10b-

598 h). CanESM5-CanOE shows a similar overall spatial pattern to other models, and generally falls

599 in the middle of the spread, particularly regarding concentrations in the Southern Ocean. Several

600 models show extremely high concentrations in the tropical-subtropical North Atlantic (Sahara

601 outflow region). CanESM5-CanOE, along with CNRM-ESM2-1 and CESM2, has much less

602 elevated concentrations in this region, due to lower deposition or greater scavenging or both.

603 CanESM5-CanOE has its lowest concentration in the eastern subtropical South Pacific, which is

604 common to many models (Figure 12). The area of strong surface depletion is generally more

605 spatially restricted in CanESM5-CanOE than in other models, and surface dFe concentrations are

606 greater over large areas of the Pacific. Both the north-south and east-west asymmetry of

607 distribution in the Pacific is greater in CanESM5-CanOE than in most other models, some of

608 which show the South Pacific minimum extending westward across the entire basin, and others
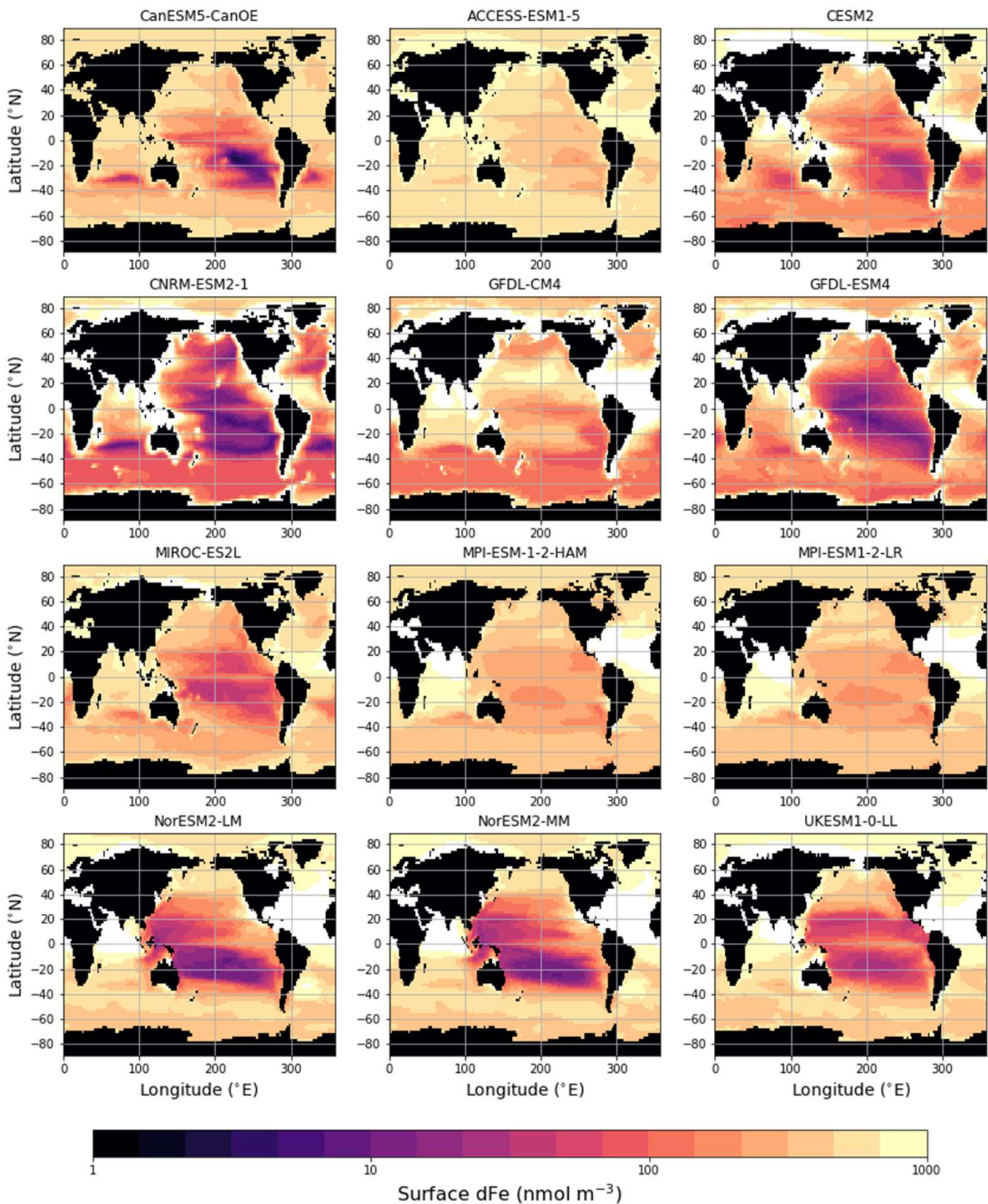
Figure 12 - Global distribution of dissolved iron (dFe) concentration (log10 of concentration in nmol m^{-3}) at the ocean surface for CanESM5-CanOE and other CMIP6 models that published this field. Concentrations exceeding 1000 nmol m^{-3} are masked white. CanESM5 is not included because it does not have prognostic iron.
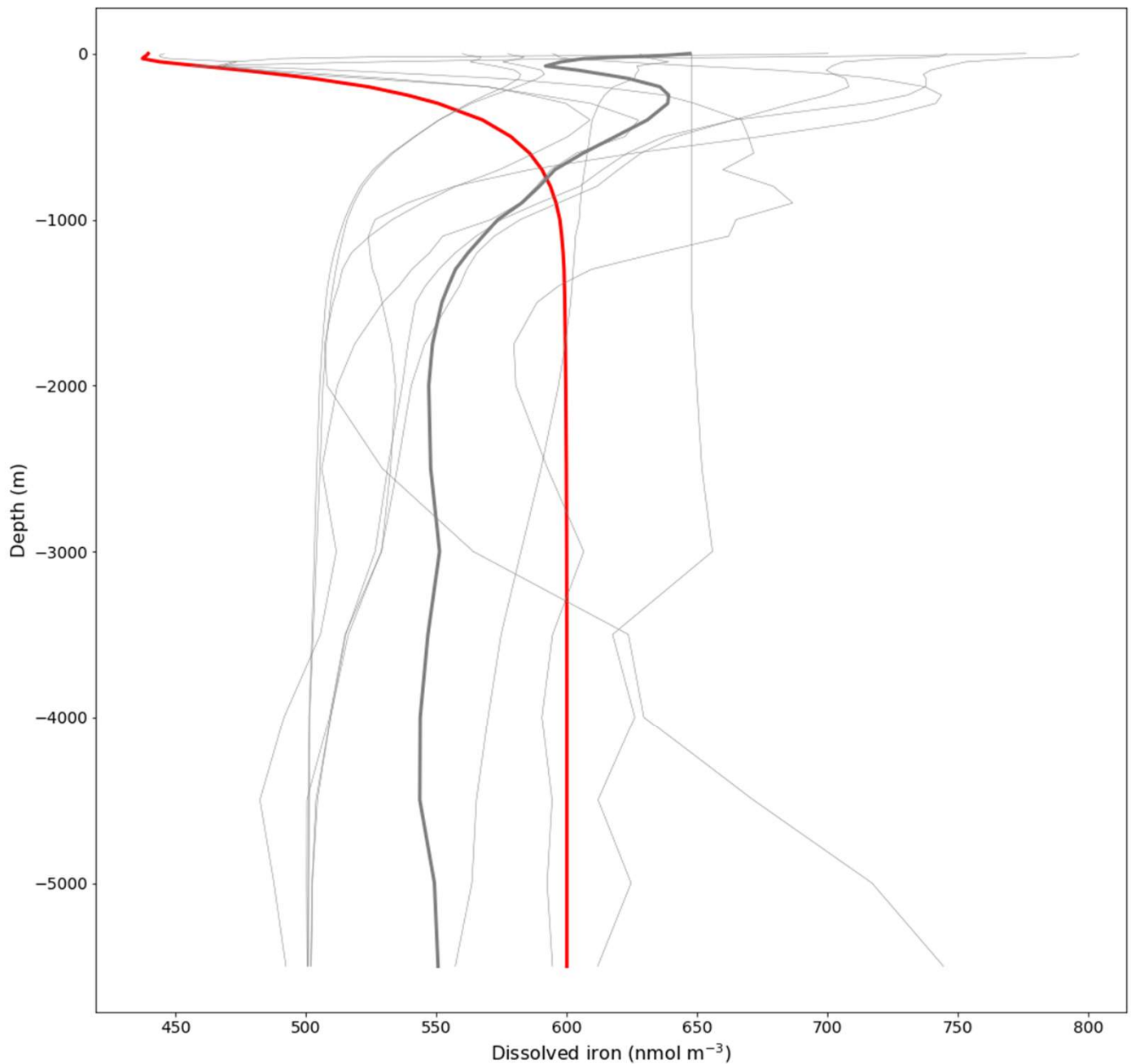
Figure 13 - Global mean depth profiles of dissolved iron concentration for CanESM5-CanOE and other CMIP6 models that published this field. GFDL-CM4 is excluded because it has very high concentrations (>2000 nmol m^{-3}) near the surface. Thick red line represents CanESM5-CanOE, thin grey lines individual CMIP6 models, and the thick grey line the model ensemble mean (excluding CanESM5-CanOE and GFDL-CM4).

611   into the Northern Hemisphere. Only in CESM2 is this minimum similarly limited to the

612   southeast Pacific.

613

614   The mean depth profiles of dFe are shown in Figure 13. Some models show more of a "nutrient-

615   type" (increasing with depth due to strong near-surface biological uptake and subsequent

616   remineralization) profile, some a more "scavenged-type" (maximal at the surface, declining with

617   depth) profile (cf. Li, 1991; Nozaki, 2001), and others a hybrid profile (increasing downward but

618   with a surface enrichment). CanESM5-CanOE is at the "nutrient-type" end of spectrum with a

619   generally monotonic increase with depth to a near-constant deep-water concentration of 0.6 nM

620   and a very slight near-surface enrichment (see also Supplementary Figures S10b,c).

621

622   Mean surface nitrate and dFe concentrations for selected ocean regions are shown in Figure 14.

623   CanESM5-CanOE shows concentrations that are within the range of CMIP6 models, although in

624   some cases at the higher or lower end. Surface nitrate concentrations generally compare

625   favourably with the observation-based climatology, but are biased low in HNLC regions other

626   than the Southern Ocean. These biases are not necessarily a consequence of having too much or

627   too little iron. For example, in the Southern Ocean CanESM5-CanOE has among the highest

628   surface nitrate concentrations, but it also has some of the highest dFe concentrations, and the

629   high nitrate bias is present in CanESM5 as well. Comparisons with the limited GEOTRACES

630   data available suggest that near surface dFe concentrations in the Southern Ocean are biased high

631   rather than low in CanESM5-CanOE (not shown). One region where there does seem to be a

632   strong correlation between surface nitrate and dFe concentrations is the western subarctic

633   Pacific. All but two models (CNRM-ESM2-1, NorESM2-LM) fall along a spectrum from high
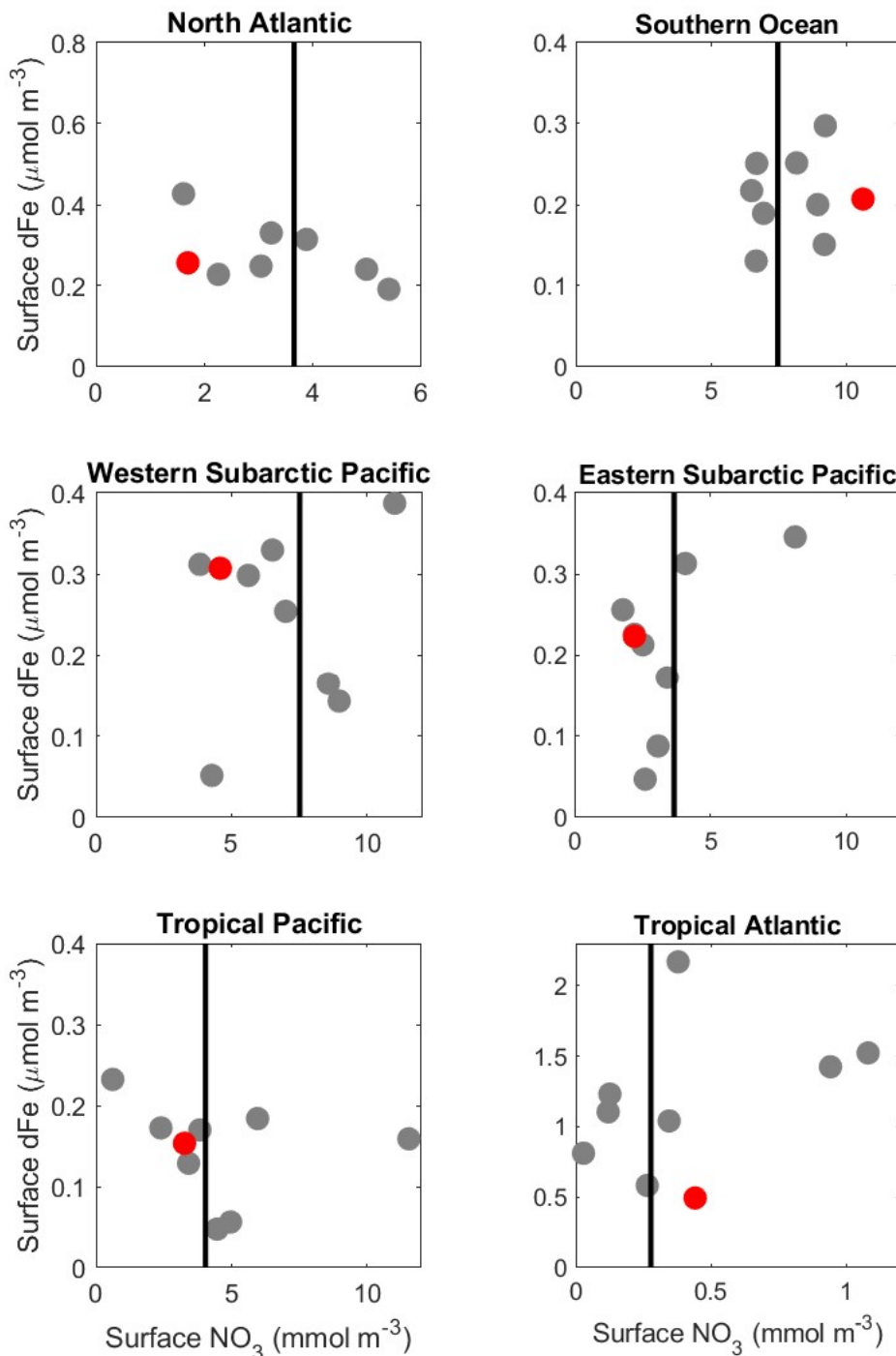
Figure 14 - Mean surface nitrate (NO3) vs. dissolved iron (dFe) concentrations in different oceans, including the major high nutrient / low chlorophyll (HNLC) regions. CanESM5-CanOE is shown as a red dot and other CMIP5 models as grey dots (CanESM5 is not included because it does not have iron). Observed NO3 is shown as a vertical black line as there are no observational estimates of dFe concentration. For GFDL-CM4, nitrate is estimated as phosphate x 16. Region definitions are given in Supplementary Table S5 and Supplementary Figure S5.
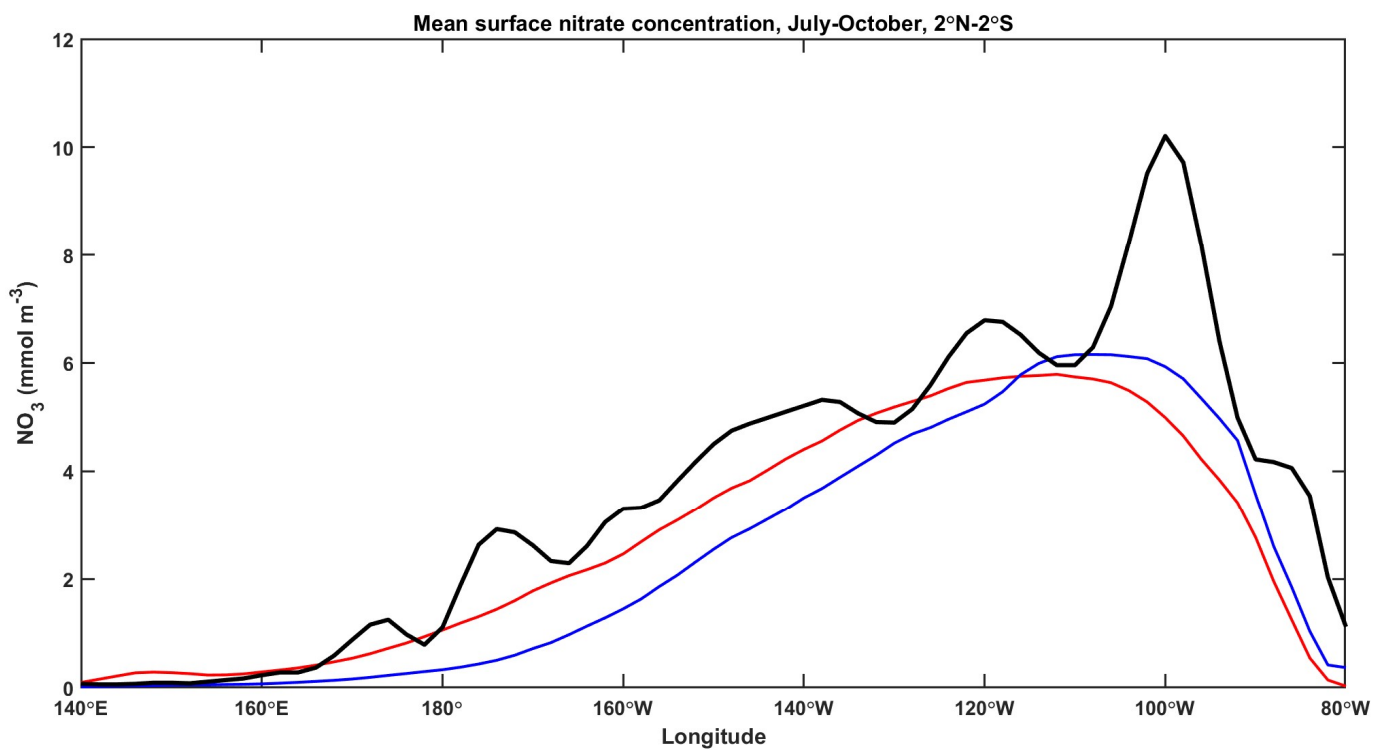
Figure 15 - Surface nitrate (NO3) concentrations along the Pacific equator (mean from 2°S-2°N) during the upwelling season (June-October) for CanESM5-CanOE (red), CanESM5 (blue), and WOA2018 observations (black).

636   Fe / low nitrate to low Fe / high nitrate. CanESM5-CanOE falls near the high Fe / low nitrate end

637   of the range.

638

639   Surface nitrate concentrations along the Pacific equator during the upwelling season (June-

640   October) for CanESM5 and CanESM5-CanOE are shown in Figure 15. The range of other

641   CMIP6 models is not shown here because it is large and therefore adds little information (see

642   Figure 11 and Supplementary Figure S6). CanESM5-CanOE better represents the east-west

643   gradient, while CanESM5 has slightly higher concentrations in the core upwelling region. Both

644   models underestimate the highest concentrations around 100°W. Although some localized

645   maxima in this data product are due to undersampling, equatorial upwelling is strong at this

646   location (e.g., Lukas, 2001) and the spatial coherence of the data strongly suggests that this

647   maximum accurately reflects reality. It should be noted that CanESM5 iron limitation is

648   calculated from a version of the same data product; however, the Fe mask is based on the

649   minimum nitrate concentration over the annual cycle, whereas the data shown here are for the

650   upwelling season.

651

652   **3.4 Plankton biomass, detritus, and particle flux**

653

654   The relative abundance of the four plankton groups are shown in Figure 16 for a range of ocean

655   regions. Both CanESM models mostly compare favourably with observation-based estimates of

656   phytoplankton biomass, except in the tropics where CanESM5-CanOE has very high biomass.

657   Both CanESM models have low phytoplankton biomass in the North Atlantic. In the North

658   Pacific and the Southern Ocean, CanESM5-CanOE reproduces the observation-based estimates
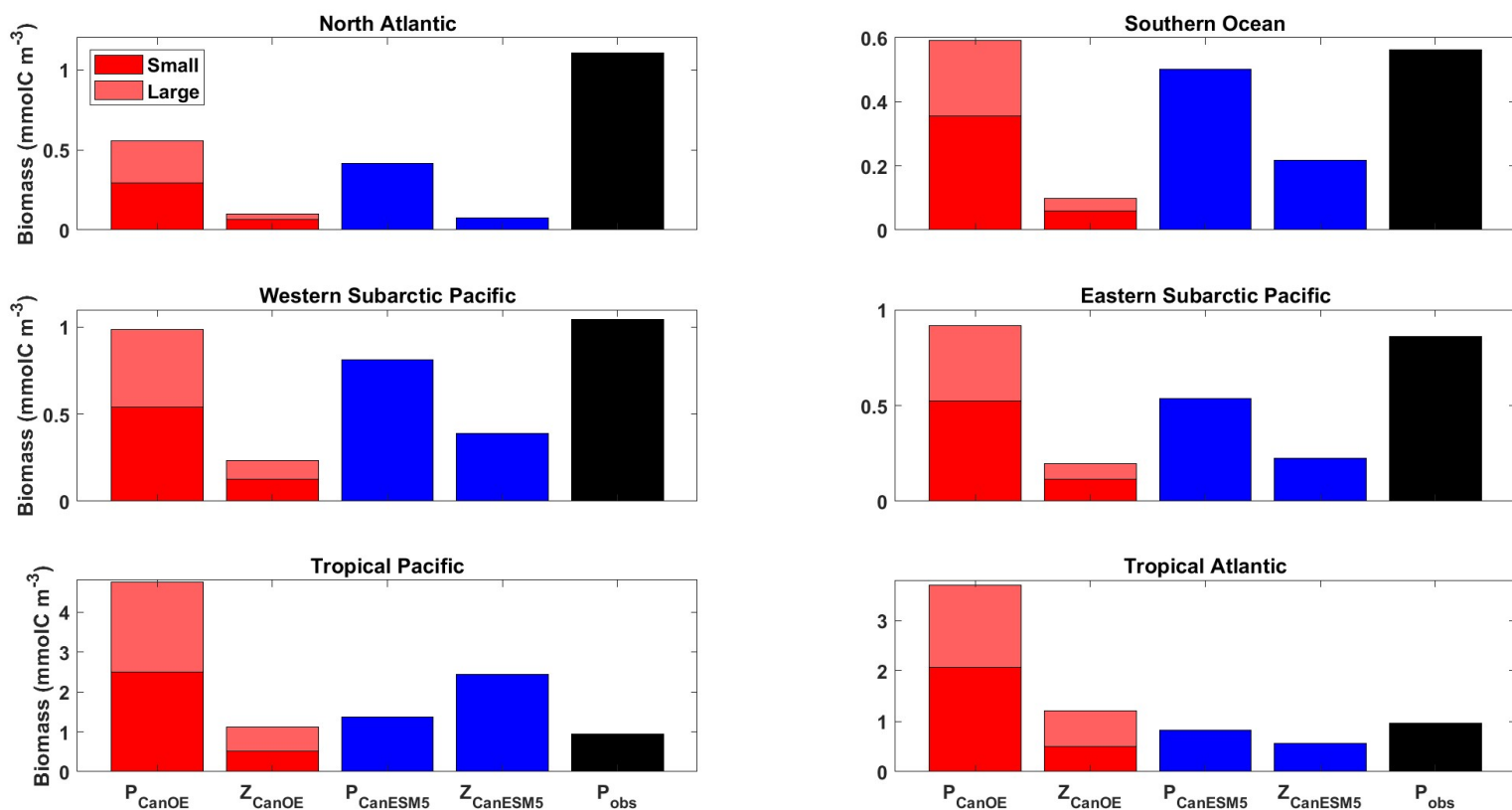
Figure 16 - Annual mean surface ocean concentration of large and small phytoplankton and zooplankton in CanESM5-CanOE (red) and of phytoplankton and zooplankton in CanESM5 (blue) for the representative ocean regions shown in Figure 14. Observational estimates (black) are for phytoplankton biomass calculated from satellite ocean colour estimates of surface chlorophyll (SeaWiFS/MODIS; Tesdal et al. 2016), assuming a carbon-to-chlorophyll ratio of 50 g/g. Region definitions are given in Supplementary Table S5 and Supplementary Figure S5.

660 well, and CanESM5 slightly less well. The general pattern is that large and small phytoplankton

661 have similar abundance, and are substantially more abundant than zooplankton.

662

663 Part of the rationale for multiple food chains is that they better represent the way that actual

664 plankton communities adapt to different physical ocean regimes and therefore are better able to

665 simulate distinct ocean regions with a single parameter set (e.g., Chisholm, 1992; Armstrong,

666 1994; Landry et al., 1997; Friedrichs et al., 2007). The expectation is that small phytoplankton

667 will be more temporally stable and large phytoplankton will fluctuate more strongly between

668 high and low abundances. The mean annual cycles of surface chlorophyll largely conform to this

669 pattern, e.g., in the North Atlantic and the western subarctic Pacific large phytoplankton are

670 dominant in summer and much more variable over the seasons (Figure 17). Compared to

671 observations, CanESM5 models underestimate the amplitude of the seasonal cycle in the North

672 Atlantic and overestimate it in the North Pacific. CanESM5 shows a stronger and earlier North

673 Atlantic spring bloom compared to CanESM5-CanOE; the observations are in between the two

674 in terms of timing, and both models underestimate the amplitude (Figure 17). In the tropics, the

675 seasonal cycle is weak. CanESM5-CanOE in the tropical Atlantic shows the expected seasonal

676 cycle but not the expected dominance of large phytoplankton in summer. CanESM5-CanOE

677 generally overestimates the total near surface chlorophyll in both the tropical Pacific and the

678 tropical Atlantic.

679

680 Zooplankton biomass (especially microzooplankton) is also somewhat difficult to test against

681 observations, but our model concentrations appear to be biased low. Stock et al. (2014) estimated

682 depth-integrated biomass of phytoplankton, mesozooplankton, and microzooplankton for a range
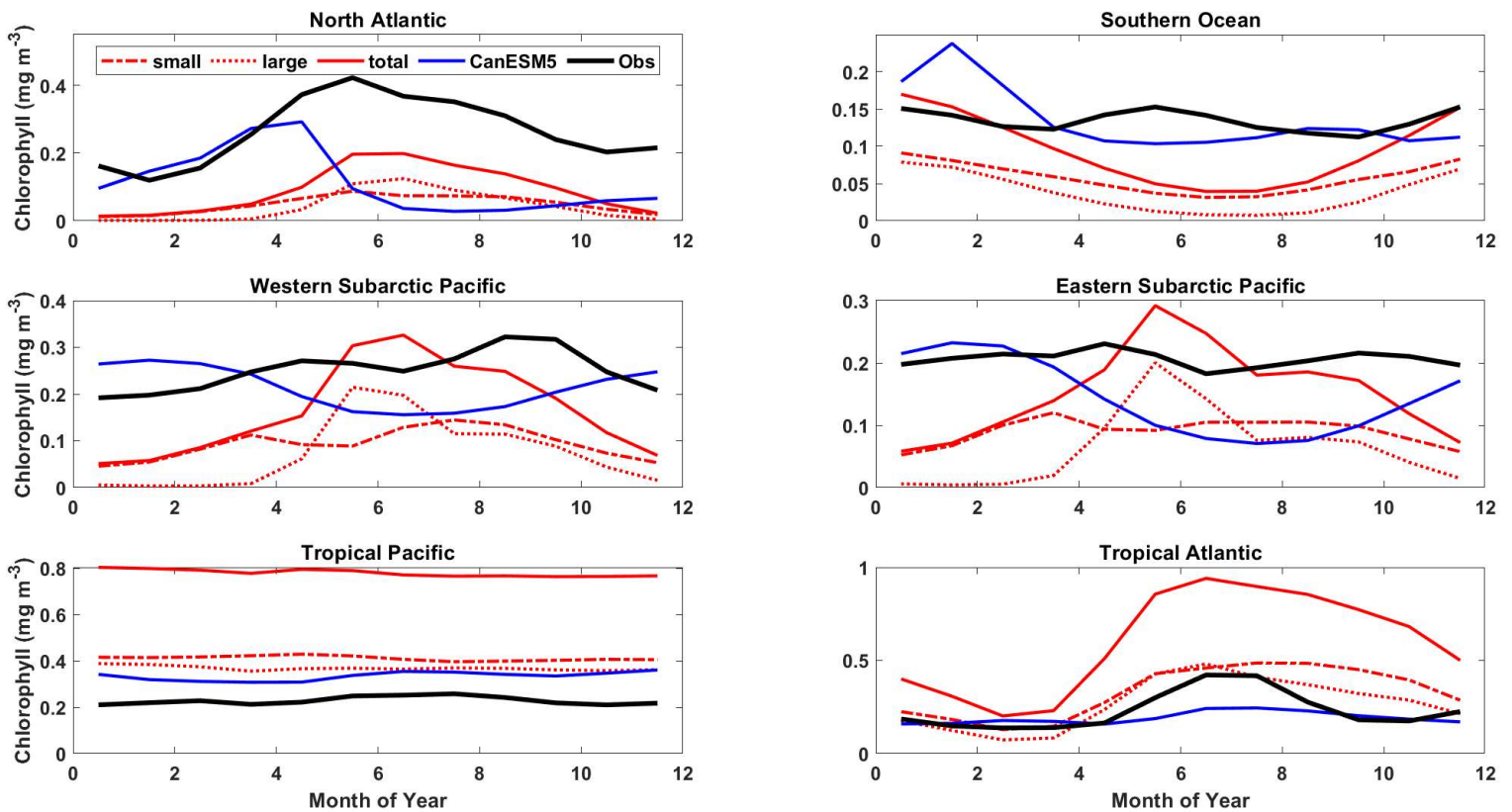
Figure 17 - Mean annual cycle of surface chlorophyll for the representative ocean regions shown in Figures 14 and 16. CanESM5-CanOE large and small phytoplankton concentrations are shown separately and combined (red) along with CanESM5 (blue) and observational estimates (black). Region definitions are shown in Supplementary Table S5 and Supplementary Figure S5.

684   of oceanic locations in which intensive field campaigns have occurred (estimates of

685   microzooplankton biomass are relatively sparse). They found that in most locations

686   phytoplankton and (combined) zooplankton biomass are of comparable magnitude, whereas in

687   CanESM5-CanOE zooplankton biomass is consistently lower (Figure 16). The global integral

688   biomass of mesozooplankton is about an order of magnitude less than the 0.19 PgC estimated by

689   Moriarty and O'Brien (2013). The CanESM5 total of 0.14 Pg is relatively close to the Moriarty

690   estimate but implicitly includes microzooplankton.

691

692   Surface chlorophyll and POC for CanESM5-CanOE and for ocean colour observational data are

693   shown in Figure 18 (POC in the model is the sum of phytoplankton, microzooplankton, and

694   detrital carbon). The observations have a lower limit for POC that is not present in the model

695   (~17 mgC m^{-3}), which is unsurprising given the processes neglected in the model, i.e., in regions

696   of very low chlorophyll there is still substantial dissolved organic carbon, bacteria that consume

697   it, and microzooplankton that consume the bacteria and produce particulate detritus. The

698   observational data show a fairly linear relationship at low concentrations, but with a curvature

699   that implies a greater phytoplankton fraction in more eutrophic environments (cf. Chisholm,

700   1992). The model, by contrast, shows a fairly linear relationship over the whole range of

701   concentrations. In other words, the phytoplankton share of POC is higher and more constant in

702   the model than in the observations. The living biomass (phytoplankton + microzooplankton)

703   fraction of total POC in CanOE is generally in excess of 50% (not shown), which is implausible

704   for a real-world oceanic microbial community (e.g., Christian and Karl, 1994) but consistent

705   with the relatively low rates of export from the euphotic zone.

706
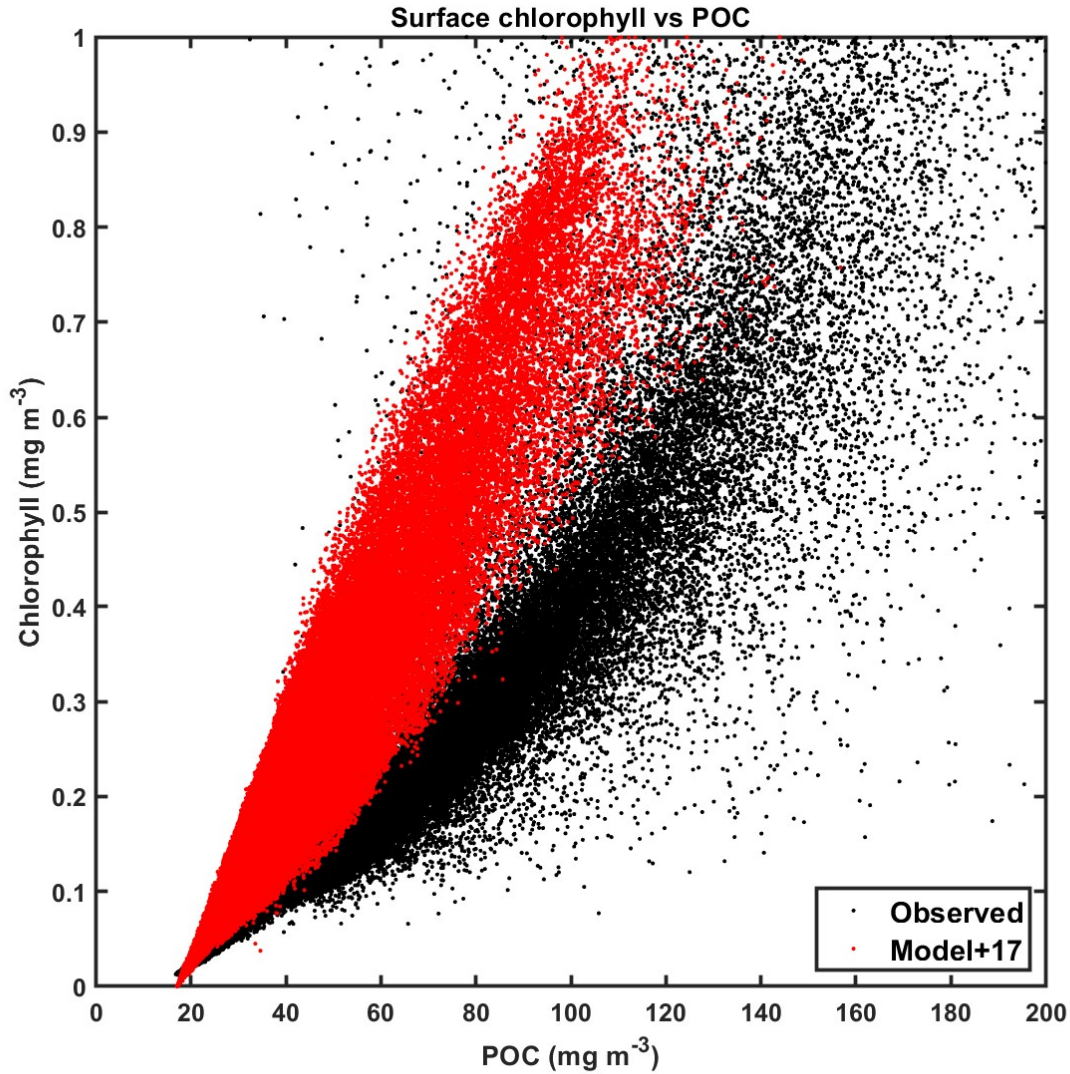
Figure 18 - Climatological surface particulate organic carbon (POC) vs. chlorophyll for CanESM5-CanOE (red) and observations (black). Data are for all ocean grid points (2x2° uniform global grid) for all months of the year where observational data are available. Model POC is offset 17 mg m^{-3} for illustrative purposes. Chlorophyll concentrations >1 mg m^{-3} are excluded as they largely represent coastal areas poorly resolved by coarse resolution global ocean models.
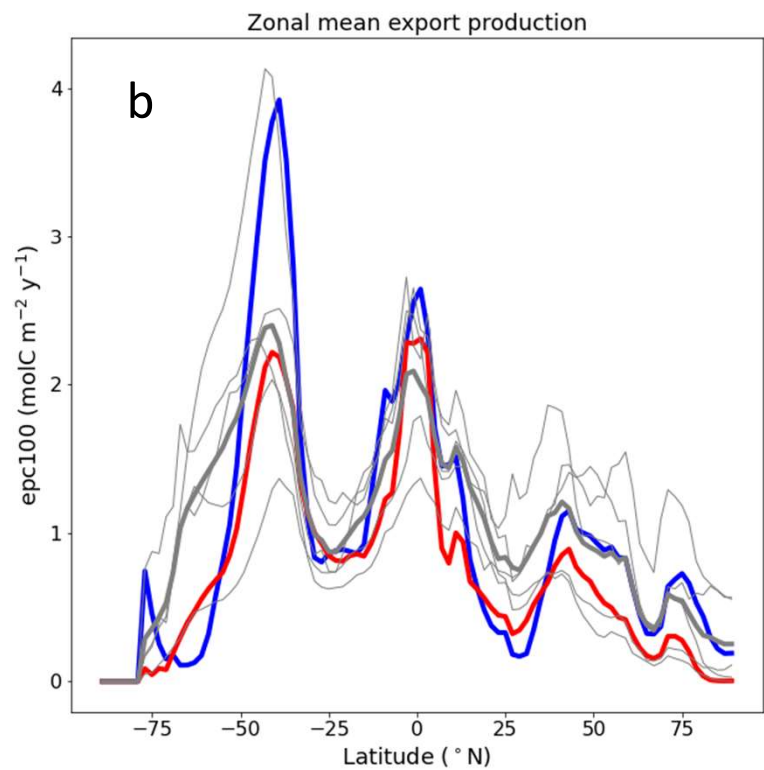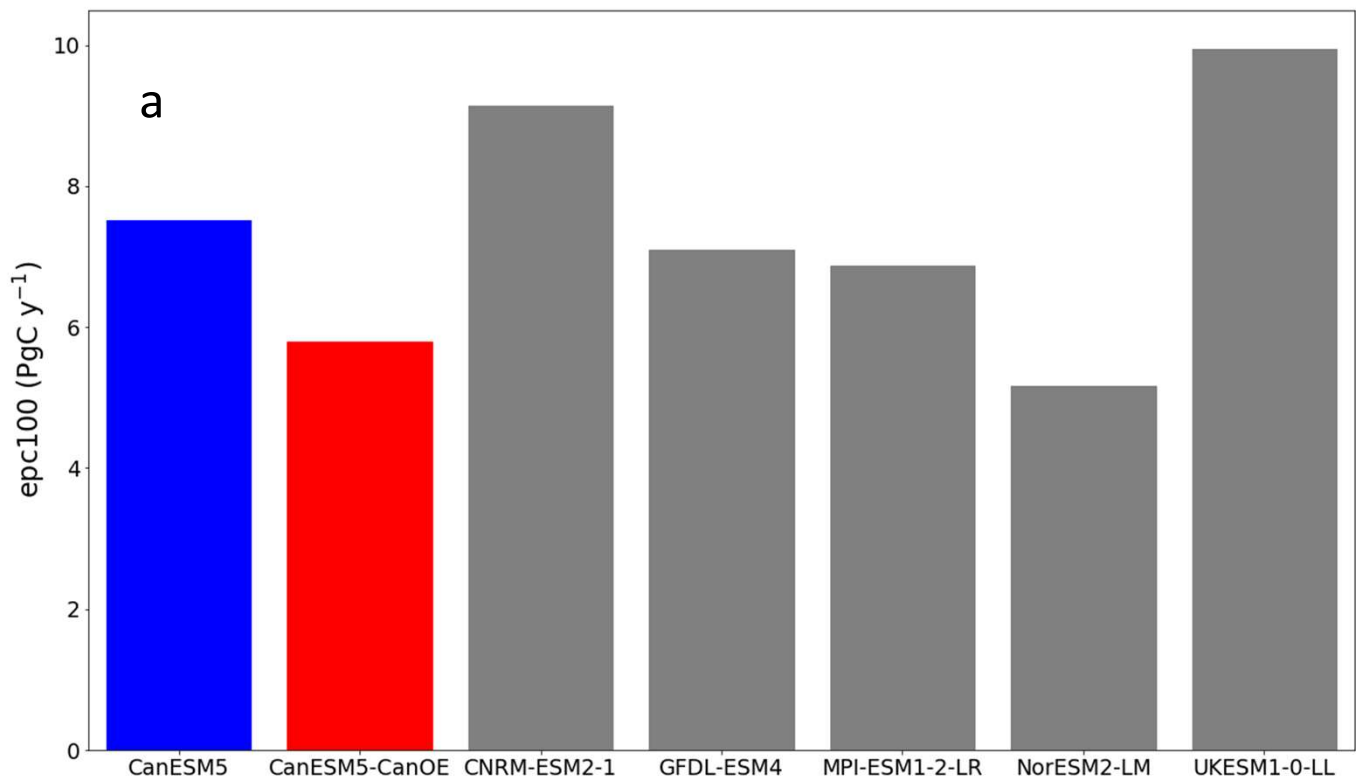
Figure 19 - (a) Global total export production (epc100) in PgC y^{-1} (b) and zonal mean export production in molC m^{-2} y^{-1} according to selected CMIP6 models (mean for 1985-2014 of historical experiment). Thick red line represents CanESM5-CanOE, thick blue line CanESM5, thin grey lines individual CMIP6 models, and thick grey line the model ensemble mean (excluding CanESM5 and CanESM5-CanOE).

710   Export production for a range of CMIP6 models is shown in Figure 19a. CanESM5-CanOE is at

711   the low end of the range. Observations are not shown because the range of observational

712   estimates covers the entire range of model estimates (e.g., Siegel et al., 2016). Note also that

713   CanESM5 export is quite a bit lower than in CanESM2, which is relatively high for CMIP5

714   models (not shown). The difference between CanESM2 and CanESM5 is attributable primarily

715   to different circulation, although the different initialization fields for nitrate might also play a

716   small role. The lower rate in CanESM5-CanOE is consistent with the above results regarding

717   plankton community structure (e.g., the concentration of detritus is generally low compared to

718   living biomass), as well as the lower sinking rate for small detritus. The latitudinal distribution of

719   export is shown in Figure 19b. CanESM5 shows very high export in the mid-latitudes of the

720   Southern Ocean, similar to CanESM2 (not shown). Both CanESM5 and CanESM5-CanOE show

721   latitudinal patterns consistent with the range of other CMIP6 models. CanESM5 has slightly

722   greater export in the equatorial zone; in both CanESM5 and CanESM5-CanOE the equatorial

723   enrichment attenuates very rapidly with latitude and the rates are low in the subtropics.

724

725   **3.5 Historical trends**

726

727   Cumulative ocean uptake of CO_2 is shown in Figure 20 for the historical experiment (1850-

728   2014). CanESM models are biased low relative to observation based estimates (~145 PgC, see

729   Friedlingstein et al., 2020) and the MEM (144 PgC, Figure 20), but fall well within the spread of

730   CMIP6 models. Some of the difference may be attributable to differences in the way cumulative

731   uptake is calculated in models vs observations (Bronselaer et al., 2017), although this should

732   apply to other CMIP6 models as well. CanESM5-CanOE has lower cumulative uptake than
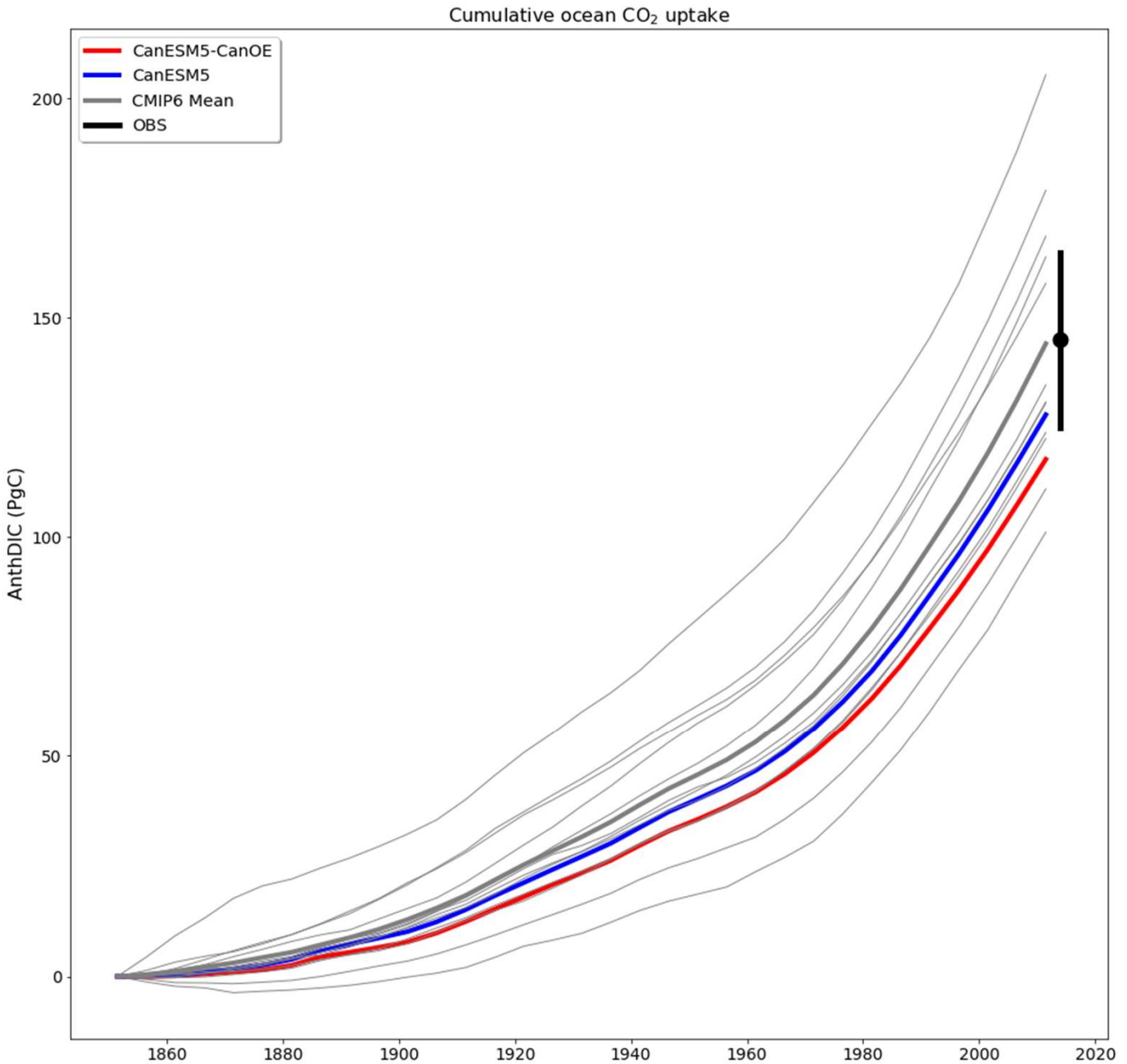
Figure 20 - Cumulative ocean uptake of carbon dioxide (CO_2) as anthropogenic dissolved inorganic carbon (AnthDIC) in PgC over the course of the historical experiment (1850-2014). Data are shown as successive five-year means. CMIP6 mean (thick grey line) indicates ensemble mean for CMIP6 models (thin grey lines) excluding CanESM5 (blue) and CanESM5-CanOE (red). An observation-based estimate of 145±20 PgC (Friedlingstein et al., 2020) is shown for nominal year 2014 (black).
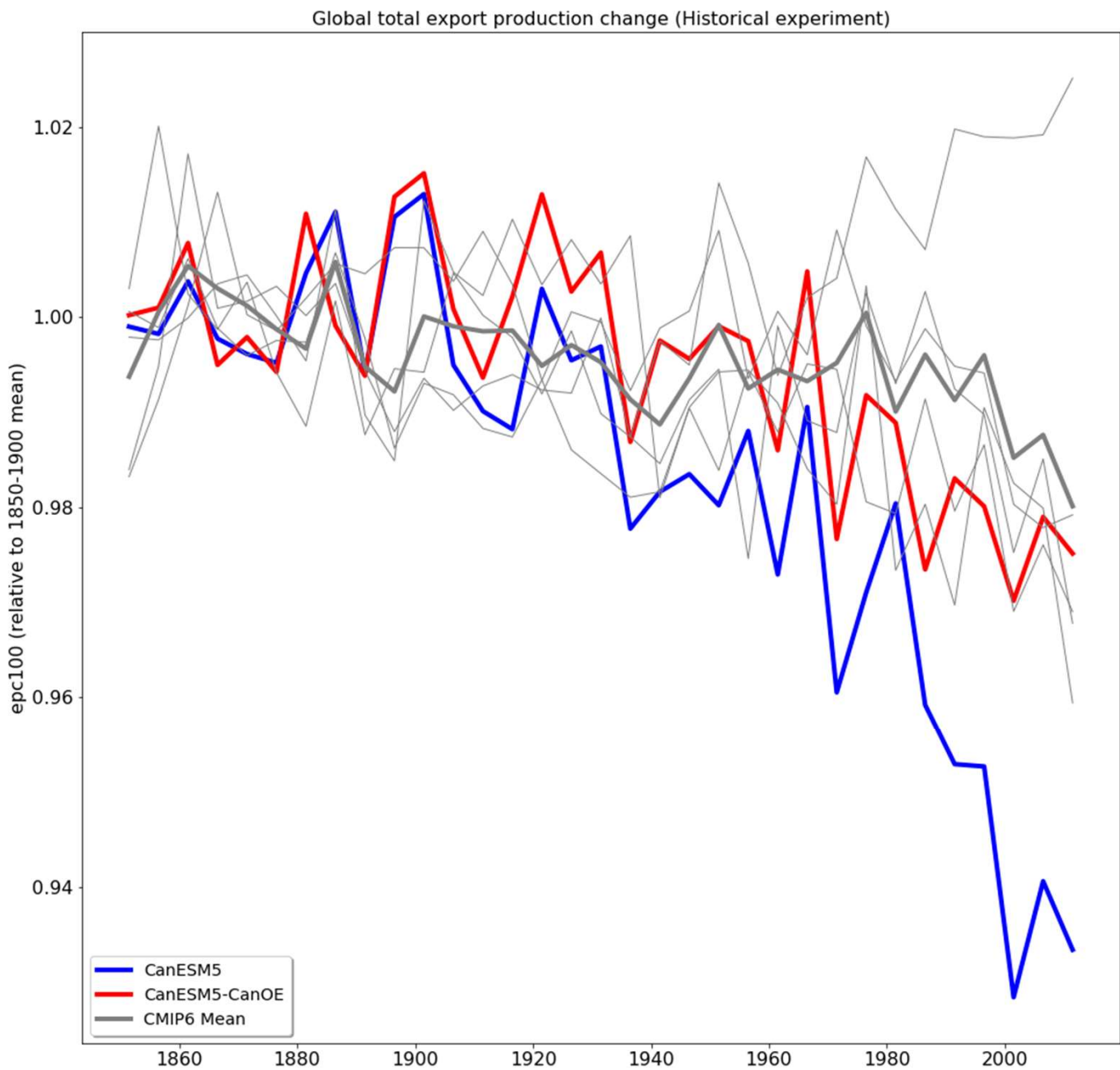
Figure 21 - Change in export production (epc100) over the course of the historical experiment (1850-2014), normalized to the 1850-1900 mean. Data are shown as successive five-year means. Thick red line represents CanESM5-CanOE, thick blue line CanESM5, thin grey lines other CMIP6 models, and thick grey line the ensemble mean of non-CanESM models.

735 CanESM5 by ~10 PgC. As the models were not fully equilibrated when the historical run was

736 launched, this difference does not necessarily arise from the biogeochemical model structure;

737 part of the difference can be attributed to differences in the spinup (cf. Séférian et al., 2016). The

738 drift in the piControl experiment over the 165 years from the branching off of the historical

739 experiment is -10.0 PgC in CanESM5-CanOE and -5.1 PgC in CanESM5 (see Supplementary

740 Table S6), so drift accounts for about half (48%) of the difference in net ocean CO_2 uptake. The

741 spatial distribution of anthropogenic DIC is very similar between CanESM5 and CanESM5-

742 CanOE (Supplementary Figure S7). CanESM5 and CanESM5-CanOE show a high bias in near

743 surface DIC relative to alkalinity (a measure of the ocean's capacity to absorb CO_2) in the mid-

744 latitudes of both hemispheres (Supplementary Figure S8), which may in part explain the weak

745 uptake of CO_2.

746

747 The long-term trend in global total export production is shown in Figure 21. The model values

748 must be normalized in order to compare trends, since the differences among means are large

749 compared to the changes over the historical period (Figure 19). Such trends are difficult or

750 impossible to meaningfully constrain with observations, but the general expectation has been that

751 export will decline somewhat due to increasing stratification (e.g., Steinacher et al., 2010).

752 CanESM5 shows a greater decline than most other CMIP6 models, while CanESM5-CanOE is

753 more similar to non-CanESM models. The change in CanESM5 is geographically widespread

754 and not concentrated in a specific region or regions: export is maximal in the tropics and the

755 northern and southern mid-latitudes (Figure 19b) and declines over the historical period in all of

756 these regions (Supplementary Figure S9). In CanESM5-CanOE, export declines in the same

757 regions, but the magnitude of the change is smaller, and in the Southern Ocean increases and
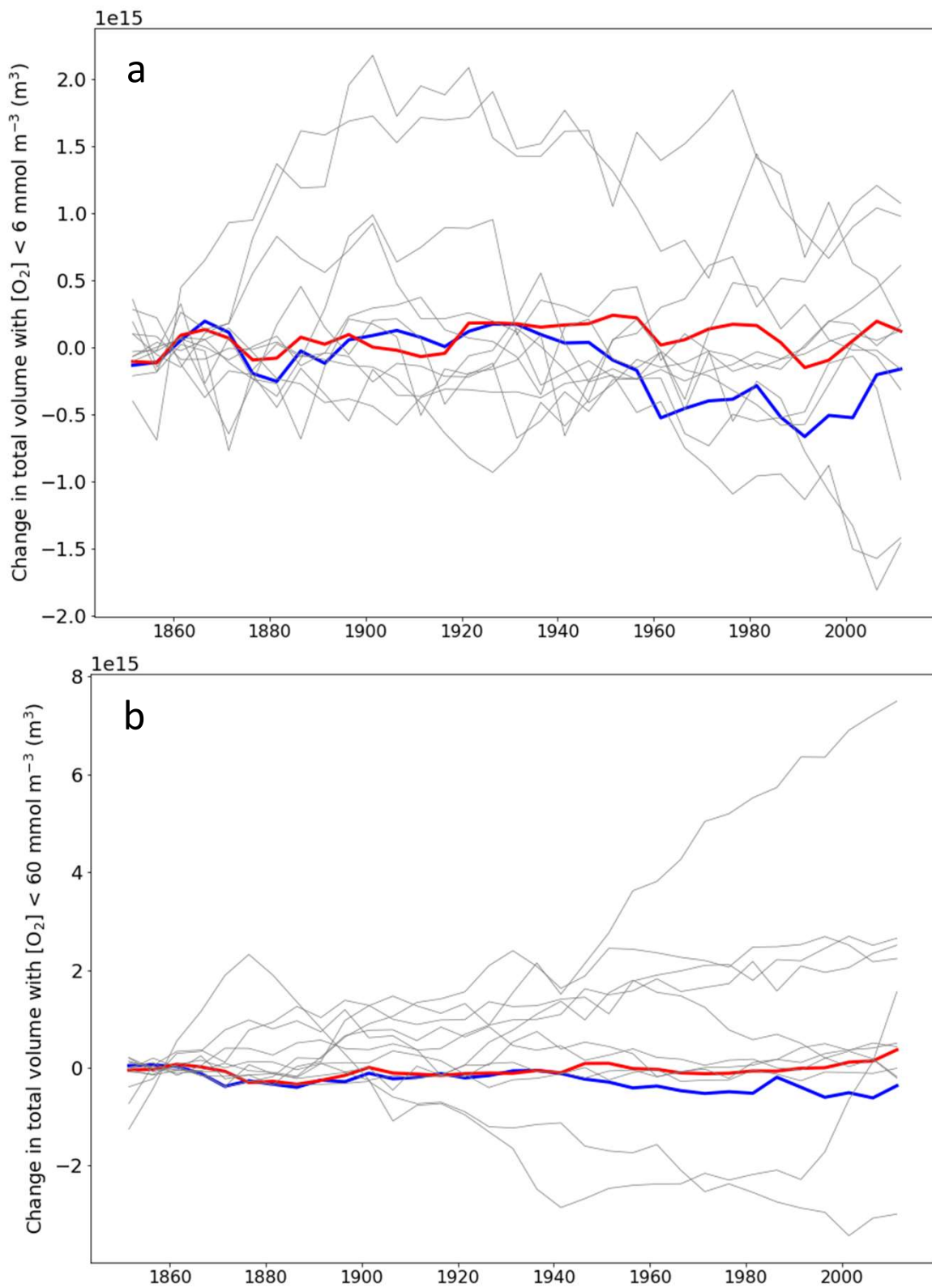
Figure 22 - (a) Change in total ocean volume with oxygen (O$_2$) concentration less than (a) 6 mmol m^{-3} and (b) 60 mmol m^{-3} over the course of the historical experiment (1850-2014), normalized to the 1850-1870 mean. Data are shown as successive five-year means. Thick red line represents CanESM5-CanOE, thick blue line CanESM5, and thin grey lines other CMIP6 models.

759   decreases in different latitude bands largely offset each other.

760

761   The trend in the volume of ocean water with O_2 concentration less than 6 or 60 mmol m^{-3} is

762   shown in Figure 22. Again, the totals are normalized to a value close to the preindustrial, as the

763   differences among models are large (Figure 5). For the volume with <60 mmol m^{-3}, CanESM

764   models show relatively little change; in CanESM5 the volume actually declines slightly, while in

765   CanESM5-CanOE it increases, but the total change is <1% in each case. As with the baseline

766   volumes, the range among models is large, with one model showing an increase approaching

767   10% of the total volume estimated for WOA2018 (Figures 5b and 22b). For the volume with <6

768   mmol m^{-3} (Figure 22a), CanESM models are among the most stable over time. In CanESM5, the

769   volume again declines, although this is within the range of internal variability. Again some

770   models show fairly large excursions, but in this case none shows a strong secular trend over the

771   last half-century.

772

773   **4. Discussion**

774

775   CanESM5 and CanESM5-CanOE are new coupled ocean-atmosphere climate models with

776   prognostic ocean biogeochemistry. The two have the same physical climate (in experiments with

777   specified atmospheric CO_2) and differ only in their ocean biogeochemistry components.

778   CanESM5-CanOE has a much more complex biogeochemistry model including a prognostic iron

779   cycle. We have presented results that assess how these two models simulate the overall

780   distribution of major tracers like DIC, alkalinity, nitrate and oxygen, as well as analyses of the

781   interaction of the iron and nitrogen cycles, plankton community structure, export of organic

782   matter from the euphotic zone, and historical trends over 1850-2014.

783

784   The overall distribution of major tracers indicates that both models do a reasonable job of

785   simulating both biogeochemical (e.g., export and remineralization of organic matter) and

786   physical (e.g., deep and intermediate ocean ventilation) processes. The volume of ocean with

787   oxygen concentration below 6 or 60 μM compares favourably with other CMIP6 models (Figure

788   5), and is among the most stable over historical time (Figure 22). CanESM5-CanOE has a

789   substantially lower volume of water with $[O_2]$<6 μM than CanESM5 and much closer to

790   observation-based estimates (Figure 22a). Both models are biased slightly low in terms of

791   historical uptake of anthropogenic CO_2, which may indicate weak Southern Ocean upwelling or

792   too shallow remineralization of DIC or both (Figure 20). The spatial distribution of

793   anthropogenic DIC is very similar between the two models (Supplementary Figure S7), which is

794   expected as it is mainly a function of the physical ocean model circulation. However, CanESM5

795   has higher concentrations in the main areas of accumulation, particularly the North Atlantic and

796   the Southern Ocean. This probably indicates more efficient removal and export of 'natural' DIC

797   by the plankton, particularly in the Southern Ocean upwelling zone (Figure 19), and deeper

798   average remineralization, with the caveat that the preindustrial control simulations had different

799   degrees of equilibration when the historical experiment was launched (cf. Séférian et al., 2016,

800   Supplementary Table S6).

801

802   Analysis of phytoplankton and zooplankton biomass concentrations show that CanESM5 and

803   CanESM5-CanOE compare somewhat favourably with available observational data but do have

804   distinct biases. In particular, both zooplankton biomass and detrital organic matter concentration

805   tend to be very low in CanESM5-CanOE; the total biomass of the plankton community and the

806   standing crop of particulate organic matter are dominated by phytoplankton (e.g., Figure 17).

807   Regional biases differ between the two models, with CanESM5-CanOE showing excessively

808   large phytoplankton biomass in the tropics. We note, however, that the seasonal cycle of

809   equatorial upwelling and the formation of the equatorial Pacific HNLC are reproduced rather

810   well by our models (e.g., Figures 11, 15 and S6), and that CanESM5-CanOE is the first CanESM

811   model to have genuinely simulated this as an emergent property (see section 3.3). In CanESM5-

812   CanOE, decoupling of large and small phytoplankton populations associated with seasonal

813   upwelling or convection (see below) is observed in some regions but not others.

814

815   Global export production is biased low, particularly in CanESM5-CanOE. This is due in part to

816   the biogeochemical model and in part to ocean circulation. CanESM5 has the same ocean

817   biology as CanESM2 but a different physical ocean model, and global ocean export production is

818   substantially lower in CanESM5. It is lower still in CanESM5-CanOE (Figure 19). We note that

819   CanESM5 performs better than CanESM2 on most metrics of physical ocean model evaluation

820   (Swart et al., 2019a), and shows a more realistic distribution of major tracers like DIC (Figure 8).

821   While the range of observation-based estimates of global ocean export production is large, and

822   encompasses the full range of CMIP5 and CMIP6 models, the change between CanESM2 and

823   CanESM5 is large. Changes in the physical ocean are not entirely independent of the

824   biogeochemistry model even when the latter is ostensibly identical. In CanESM2 and CanESM5,

825   iron limitation is specified as a spatially static 'mask' based on the observed distribution of

826   surface nitrate, and it is possible that in these two models ocean upwelling occurs in different

827   places relative to the specified boundary of the region of Southern Ocean iron imitation (Figure 3

828   of Zahariev et al., 2008). It is also possible that the lower export production in CanESM5-CanOE

829   is due to low iron supply to the surface waters of the Southern Ocean, but comparison with

830   available observations do not suggest that this is the case. Several biases are common to

831   CanESM5 and CanESM5-CanOE that relate to Southern Ocean upwelling (high Southern Ocean

832   surface nitrate concentration, low export production, weak anthropogenic CO_2 uptake) and so are

833   probably more attributable to the physical ocean model than to the Fe submodel. The difference

834   between CanESM2 and CanESM5 bears this out.

835

836   The development of CanOE was undertaken in response to some of the most severe limitations

837   of CanESM2. Many of the additional features that CanOE introduces were already in the models

838   published by other centres even in CMIP5. In addition to CMOC (Zahariev et al., 2008),

839   previous models developed by members of our group include Denman and Peña (1999; 2002),

840   Christian et al. (2002a; 2002b), Christian (2005), and Denman et al. (2006). Christian et al.

841   (2002a) had a prognostic Fe cycle and multiple phytoplankton and zooplankton species, but had

842   fixed elemental ratios. Christian (2005) incorporated a cellular-regulation model, but only for a

843   single species and without Fe limitation. Christian (2005) had prognostic chlorophyll whereas

844   Denman and Peña (1999; 2002) and Christian et al. (2002a) used an irradiance-dependent

845   diagnostic formulation. Christian et al. (2002a) used multiplicative (Franks et al., 1986) grazing,

846   which creates stability in predator-prey interactions but severely limits phytoplankton biomass

847   accumulation under nutrient-replete conditions.

848

849 One of the most important lessons from Christian et al. (2002a; 2002b) was that when a fixed

850 Fe/N ratio is employed, sensitivity to this parameter is extreme. Because Fe cell quotas are far

851 more variable than N, P, or Si quotas, treating this parameter as constant results in the specified

852 value influencing the overall solution far more than any other parameter. CanESM5-CanOE

853 largely succeeded in creating a prognostic Fe-N limitation model that produces HNLC conditions

854 in the expected regions (Figures 10, 11, 14, 15, S6), although surface nitrate concentration is low

855 relative to observation-based estimates in some cases. External Fe sources and scavenging

856 parameterizations will be revisited and refined in future versions. In CanESM5-CanOE the

857 scavenging model is very simple, with distinct regimes for concentrations greater or less than 0.6

858 nM; scavenging rates are very high above this threshold which causes deep-water concentrations

859 to converge on this value. The generally nutrient-like profile suggest that in CanOE the

860 scavenging rate is quite low for concentrations below 0.6 nM (Figure 13; see also Supplementary

861 Figure S10h). We note that the aeolian mineral dust deposition field employed here is derived

862 from the CanESM atmosphere model; these processes are not presently interactive but could be

863 made so in the future.

864

865 A particular issue with CanESM2 was that extremely high concentrations of nitrate occurred

866 under the EBC upwelling regions. This error resulted from spreading denitrification out over the

867 ocean basin so that introduction of new fixed N from N_2 fixation would balance denitrification

868 losses within each vertical column, whereas in the real world denitrification is highly localized in

869 the low oxygen environments under the EBCs. CanESM2 did not include oxygen, but CanESM5

870 incorporates oxygen as a 'downstream' tracer that does not feed back on other biogeochemical

871 processes. The incorporation of a more process-based denitrification parameterization in

872 CanESM5-CanOE is independent of the many other processes that are present in CanESM5-

873 CanOE but not in CanESM5: a CMOC-like model with prognostic denitrification is clearly an

874 option. We chose not to include explicit, oxygen-dependent denitrification in CanESM5 because

875 we wanted to maintain a CMOC-based model as close to the CanESM2 version as possible, and

876 because oxygen would not then be a downstream tracer that does not affect other processes.

877

878 Plankton community structure in CanESM5-CanOE is somewhat biased toward high

879 concentrations of phytoplankton, low concentrations of zooplankton and detritus, and low export

880 (Sect. 3.4). In the development phase, a fair number of experiments were conducted with various

881 values of the grazing rates and detritus sinking speeds. A wide range of values of these

882 parameters was tested, with no resulting improvement in the overall results. Possibly the detrital

883 remineralization rates are too high, although primary production is also on the low end of the

884 CMIP6 range (not shown), and would probably decline further if these rates were decreased. The

885 model was designed around the Armstrong (1994) hypothesis of 'supplementation' vs

886 'replacement', i.e., small phytoplankton and their grazers do not become much more abundant in

887 more nutrient-rich environments but rather stay at about the same level and are joined by larger

888 species that are absent in more oligotrophic conditions (see also Chisholm, 1992; Landry et al.,

889 1997; Friedrichs et al., 2007). The results presented here suggest that this was partially achieved,

890 but further improvement is possible (Figure 17).

891

892 As to whether the gains in skill with CanESM5-CanOE justify the extra computational cost,

893 Taylor diagrams (Figures 4, 8, 9, and Supplementary Figure S4) show a modest but consistent

894 gain in skill at simulating the major biogeochemical species (O_2, DIC, alkalinity) across

895   variables and depths, especially for alkalinity at mid-depths (Supplementary Figure S4), for

896   which CanESM5 displays the least skill relative to other fields or depths. Other processes that are

897   highly parameterized in CanESM5, such as calcification and $CaCO_3$ dissolution, were not

898   addressed in detail in this paper, but are an important factor in determining the subsurface

899   distribution of alkalinity. Again, we emphasize that we are simulating as an emergent property of

900   a process-based model something that is parameterized in CanESM5 (as previously noted for

901   surface nitrate concentration in HNLC regions), and doing at least as well in terms of model

902   skill. As a general rule, the potential for improving skill and achieving better results in novel

903   environments (e.g., topographically complex regional domains like the Arctic Ocean and the

904   boreal marginal seas), is expected to be greater in less parameterized, more mechanistic models

905   (e.g., Friedrichs et al., 2007; Tesdal et al., 2016). Inclusion of a prognostic iron cycle and C/N/Fe

906   stoichiometry also open up additional applications and scientific investigations that are not

907   possible with CMOC.

908

909   An updated version of CanESM5 with prognostic denitrification is clearly possible. However, for

910   the reasons discussed above, a prognostic Fe cycle with a fixed phytoplankton Fe/N remains

911   problematic, and the model would still have a single detritus sinking speed and remineralization

912   length scale. We are also developing CanOE for regional downscaling applications (Hayashida,

913   2018; Holdsworth et al., 2021). The regional domains have complex topography and prominent

914   continental shelf and slope, and the single remineralization length scale in CMOC may not be

915   well suited to such an environment. The number of tracers in CanOE is not particularly large

916   compared with other CMIP6 models. We expect to further refine CanOE and its

917   parameterizations, evaluate it against new and emerging ocean data sets (e.g., GEOTRACES,

918   biogeochemical Argo), and incrementally improve CMOC (which we will maintain for a wide

919   suite of physical-climate experiments for which ocean biogeochemistry is not central to the

920   purpose). For CMIP6, we chose to keep CMOC as close to the CanESM2 version as possible.

921   This strategy allows us to quantify how much of the improvement in model skill is due to the

922   physical circulation, as is illustrated by greater skill with respect to DIC (Figure 8) and alkalinity

923   (Supplementary Figure S4), particularly at intermediate depths (400-900 m). The CanESM

924   terrestrial carbon model is also undergoing important new developments (e.g., Asaadi and Arora,

925   2021) and we expect CanESM to continue to offer a credible contribution to global carbon cycle

926   studies, as well as advancing regional downscaling and impacts science.

927

928   *Code availability*. The full CanESM5 source code is publicly available at

929   gitlab.com/cccma/canesm; within this tree the ocean biogeochemistry code can be found at

930   gitlab.com/cccma/cannemo/-/tree/v5.0.3/nemo/CONFIG/CCC_CANCPL_ORCA1_LIM_CMOC

931   or CCC_CANCPL_ORCA1_LIM_CANOE (last access: 21 September 2021). The version of the

932   code which can be used to produce all the simulations submitted to CMIP6, and described in this

933   paper, is tagged as v5.0.3 and has the associated DOI: https://doi.org/10.5281/zenodo.3251113

934   (Swart et al., 2019b).

935

936   *Data availability*. All simulations conducted for CMIP6, including those described in this paper,

937   are publicly available via the Earth System Grid Federation (source_id = CanESM5 or

938   CanESM5-CanOE). All observational data and other CMIP6 model data used are publicly

939   available.

940

941 *Author contributions.* Formulation of the overall research goals and aims: JRC, KLD, NS, NCS;

942 Implementation and testing of the model code: JRC, HH, AMH, WGL, OGJR, AES, NCS;

943 Carrying out the experiments: JRC, WGL, OGJR, AES, NCS; Creation of the published work:

944 JRC, HH, AMH, AES, NS, NCS.

945

946 *Competing interests*. The authors declare that they have no conflict of interest.

947

948 *Disclaimer*. CanESM has been customized to run on the ECCC high-performance computer, and

949 a significant fraction of the software infrastructure used to run the model is specific to the

950 individual machines and architecture. While we publicly provide the code, we cannot provide

951 any support for migrating the model to different machines or architectures.

952

953 *Acknowledgments*. This work was made possible by the combined efforts of the CCCMa model

954 development team and computing support team. We thank all of the the data contributors to and

955 developers of the observational data products, the NASA ocean colour team, and all of the

956 CMIP6 data contributors. The Python packages mocsy by Jim Orr and SkillMetrics by Peter

957 Rochford were invaluable tools in the analysis. William Merryfield and Andrew Ross made

958 useful comments on an earlier draft. Fiona Davidson helped with figure preparation. This paper

959 is dedicated to the memory of Mr. Fouad Majaess, who supported CCCMa supercomputer users

960 for many years and passed away suddenly in 2020.

961
962
963
964 **Literature Cited**
965

966

967 Arguez, A. and Vose, R.: The Definition of the Standard WMO Climate Normal The Key to
968 Deriving Alternative Climate Normals, Bulletin of the American Meteorological Society, 92,
969 699-704, 10.1175/2010BAMS2955.1, 2011.
970

971 Armstrong, R.: Grazing limitation and nutrient limitation in marine ecosystems - steady-state
972 solutions of an ecosystem model with multiple food-chains, Limnology and Oceanography, 39,
973 597-608, 1994.
974

975 Arora, V., Scinocca, J., Boer, G., Christian, J., Denman, K., Flato, G., Kharin, V., Lee, W., and
976 Merryfield, W.: Carbon emission limits required to satisfy future representative concentration
977 pathways of greenhouse gases, Geophysical Research Letters, 38, 10.1029/2010GL046270,
978 2011.
979
980

981 Arora, V., Katavouta, A., Williams, R., Jones, C., Brovkin, V., Friedlingstein, P., Schwinger, J.,
982 Bopp, L., Boucher, O., Cadule, P., Chamberlain, M., Christian, J., Delire, C., Fisher, R., Hajima,
983 T., Ilyina, T., Joetzjer, E., Kawamiya, M., Koven, C., Krasting, J., Law, R., Lawrence, D.,
984 Lenton, A., Lindsay, K., Pongratz, J., Raddatz, T., Seferian, R., Tachiiri, K., Tjiputra, J.,
985 Wiltshire, A., Wu, T., and Ziehn, T.: Carbon-concentration and carbon-climate feedbacks in
986 CMIP6 models and their comparison to CMIP5 models, Biogeosciences, 17, 4173-4222,
987 10.5194/bg-17-4173-2020, 2020.
988

989 Asaadi, A. and Arora, V.: Implementation of nitrogen cycle in the CLASSIC land model,
990 Biogeosciences, 18, 669-706, 10.5194/bg-18-669-2021, 2021.
991

992 Aumont, O., Ethe, C., Tagliabue, A., Bopp, L., and Gehlen, M.: PISCES-v2: an ocean
993 biogeochemical model for carbon and ecosystem studies, Geoscientific Model Development, 8,
994 2465-2513, 10.5194/gmd-8-2465-2015, 2015.
995

996 Babbin, A., Keil, R., Devol, A., and Ward, B.: Organic Matter Stoichiometry, Flux, and Oxygen
997 Control Nitrogen Loss in the Ocean, Science, 344, 406-408, 10.1126/science.1248364, 2014.
998

999 Bronselaer, B., Winton, M., Russell, J., Sabine, C., and Khatiwala, S.: Agreement of CMIP5
1000 Simulated and Observed Ocean Anthropogenic CO_2 Uptake, Geophysical Research Letters, 44,
1001 12298-12305, 10.1002/2017GL074435, 2017.
1002

1003 Chisholm, S.W.: Phytoplankton size, in: Primary productivity and biogeochemical cycles in the
1004 sea, edited by: Falkowski, P.G., and Woodhead A.D., Plenum, New York, 213-237, 1992.
1005

1006 Christian, J.: Biogeochemical cycling in the oligotrophic ocean: Redfield and non-Redfield
1007 models, Limnology and Oceanography, 50, 646-657, 2005.
1008

1009 Christian, J. and Karl, D.: Microbial community structure at the United States Joint Global
1010 Ocean Flux Study Station ALOHA - inverse methods for estimating biochemical indicator ratios,
1011 Journal of Geophysical Research-Oceans, 99, 14269-14276, 10.1029/94JC00681, 1994.

1012

Christian, J., Arora, V., Boer, G., Curry, C., Zahariev, K., Denman, K., Flato, G., Lee, W., Merryfield, W., Roulet, N., and Scinocca, J.: The global carbon cycle in the Canadian Earth system model (CanESM1): Preindustrial control simulation, Journal of Geophysical Research-Biogeosciences, 115, 10.1029/2008JG000920, 2010.

Christian, J. R., Verschell, M. A., Murtugudde, R., Busalacchi, A. J., and McClain, C. R.: Biogeochemical modelling of the tropical Pacific Ocean. I: Seasonal and interannual variability, Deep-Sea Research Part II-Topical Studies in Oceanography, 49, 509-543, 2002a.

Christian, J. R., Verschell, M. A., Murtugudde, R., Busalacchi, A. J., and McClain, C. R.: Biogeochemical modelling of the tropical Pacific Ocean. II: Iron biogeochemistry, Deep-Sea Research Part II-Topical Studies in Oceanography, 49, 545-565, 0.1016/s0967-0645(01)00111-4, 2002b.

Denman, K. and Pena, M.: A coupled 1-D biological/physical model of the northeast subarctic Pacific Ocean with iron limitation, Deep-Sea Research Part II-Topical Studies in Oceanography, 46, 2877-2908, 10.1016/S0967-0645(99)00087-9, 1999.

Denman, K. and Pena, M.: The response of two coupled one-dimensional mixed layer/planktonic ecosystem models to climate change in the NE subarctic Pacific Ocean, Deep-Sea Research Part II-Topical Studies in Oceanography, 49, 5739-5757, 10.1016/S0967-0645(02)00212-6, 2002.

Denman, K., Voelker, C., Pena, M., and Rivkin, R.: Modelling the ecosystem response to iron fertilization in the subarctic NE Pacific: The influence of grazing, and Si and N cycling on CO_2 drawdown, Deep-Sea Research Part II-Topical Studies in Oceanography, 53, 2327-2352, 10.1016/j.dsr2.2006.05.026, 2006.

Devol, A.H.: Denitrification including anammox, in: Nitrogen in the Marine Environment, 2nd edition, edited by: Capone, D.G., Bronk D.A., Mulholland M.R., and Carpenter E.J., Elsevier, Amsterdam, 263-301, 2008.

Dickson, A.G., Sabine, C.L., and Christian, J.R., eds.: Guide to best practices for ocean CO_2 measurements, PICES Special Publication #3, 2007

Elser, J. and Urabe, J.: The stoichiometry of consumer-driven nutrient recycling: Theory, observations, and consequences, Ecology, 80, 735-751, 10.1890/0012-9658(1999)080[0735:TSOCDN]2.0.CO;2, 1999.

Franks, P., Wroblewski, J., and Flierl, G.: Behavior of a simple plankton model with food-level acclimation by herbivores, Marine Biology, 91, 121-129, 10.1007/BF00397577, 1986.

Friedlingstein, P., O'Sullivan, M., Jones, M., Andrew, R., Hauck, J., Olsen, A., Peters, G., Peters, W., Pongratz, J., Sitch, S., Le Quere, C., Canadell, J., Ciais, P., Jackson, R., Alin, S., Aragao, L., Arneth, A., Arora, V., Bates, N., Becker, M., Benoit-Cattin, A., Bittig, H., Bopp, L., Bultan, S., Chandra, N., Chevallier, F., Chini, L., Evans, W., Florentie, L., Forster, P., Gasser, T., Gehlen,

M., Gilfillan, D., Gkritzalis, T., Gregor, L., Gruber, N., Harris, I., Hartung, K., Haverd, V., Houghton, R., Ilyina, T., Jain, A., Joetzjer, E., Kadono, K., Kato, E., Kitidis, V., Korsbakken, J., Landschutzer, P., Lefevre, N., Lenton, A., Lienert, S., Liu, Z., Lombardozzi, D., Marland, G., Metzl, N., Munro, D., Nabel, J., Nakaoka, S., Niwa, Y., O'Brien, K., Ono, T., Palmer, P., Pierrot, D., Poulter, B., Resplandy, L., Robertson, E., Rodenbeck, C., Schwinger, J., Seferian, R., Skjelvan, I., Smith, A., Sutton, A., Tanhua, T., Tans, P., Tian, H., Tilbrook, B., Van der Werf, G., Vuichard, N., Walker, A., Wanninkhof, R., Watson, A., Willis, D., Wiltshire, A., Yuan, W., Yue, X., and Zaehle, S.: Global Carbon Budget 2020, Earth System Science Data, 12, 3269-3340, 10.5194/essd-12-3269-2020, 2020.

Friedrichs, M., Dusenberry, J., Anderson, L., Armstrong, R., Chai, F., Christian, J., Doney, S., Dunne, J., Fujii, M., Hood, R., McGillicuddy, D., Moore, J., Schartau, M., Spitz, Y., and Wiggert, J.: Assessment of skill and portability in regional marine biogeochemical models: Role of multiple planktonic groups, Journal of Geophysical Research-Oceans, 112, 10.1029/2006JC003852, 2007.

Garcia, H.E., Weathers, K., Paver, C.R., Smolyar, I., Boyer, T.P., Locarnini, R.A., Zweng, M.M., Mishonov, A.V., Baranova, O.K., Seidov, D. and Reagan, J.R.: World Ocean Atlas 2018, Volume 3: Dissolved Oxygen, Apparent Oxygen Utilization, and Oxygen Saturation. A. Mishonov Technical Ed., NOAA Atlas NESDIS 83, 38pp., 2018a.

Garcia, H.E., Weathers, K., Paver, C.R., Smolyar, I., Boyer, T.P., Locarnini, R.A., Zweng, M.M., Mishonov, A.V., Baranova, O.K., Seidov, D. and Reagan, J.R.: World Ocean Atlas 2018, Volume 4: Dissolved Inorganic Nutrients (phosphate, nitrate and nitrate+nitrite, silicate). A. Mishonov Technical Ed., NOAA Atlas NESDIS 84, 35pp., 2018b.

Geider, R., MacIntyre, H., and Kana, T.: A dynamic regulatory model of phytoplanktonic acclimation to light, nutrients, and temperature, Limnology and Oceanography, 43, 679-694, 1998.

Guilyardi, E. and Madec, G.: Performance of the OPA/ARPEGE-T21 global ocean-atmosphere coupled model, Climate Dynamics, 13, 149-165, 10.1007/s003820050157, 1997.

Hayashida, H.: Modelling sea-ice and oceanic dimethylsulde production and emissions in the Arctic, PhD thesis, University of Victoria, 2018.

Holdsworth, A.M., Zhai, L., Lu, Y., and Christian, J.R.: Future changes in oceanography and biogeochemistry along the Canadian Pacific continental margin, Frontiers in Marine Science, 10.3389/fmars.2021.602991, 2021.

Jetten, M., Wagner, M., Fuerst, J., van Loosdrecht, M., Kuenen, G., and Strous, M.: Microbiology and application of the anaerobic ammonium oxidation ('anammox') process, Current Opinion in Biotechnology, 12, 283-288, 10.1016/S0958-1669(00)00211-1, 2001.

Johnson, K. S., Gordon, R. M., and Coale, K. H.: What controls dissolved iron concentrations in the world ocean?, Marine Chemistry, 57, 137-161, 10.1016/s0304-4203(97)00043-1, 1997.

1104

1105 Johnson, K., Elrod, V., Fitzwater, S., Plant, J., Chavez, F., Tanner, S., Gordon, R., Westphal, D.,
1106 Perry, K., Wu, J., and Karl, D.: Surface ocean-lower atmosphere interactions in the Northeast
1107 Pacific Ocean Gyre: Aerosols, iron, and the ecosystem response, Global Biogeochemical Cycles,
1108 17, 10.1029/2002GB002004, 2003.

1109

1110 Key, R.M., Olsen, A., van Heuven, S., Lauvset, S. K., Velo, A., Lin, X., Schirnick, C., Kozyr,
1111 A., Tanhua, T., Hoppema, M., Jutterström, S., Steinfeldt, R., Jeansson, E., Ishii, M., Perez, F. F.,
1112 and Suzuki, T.: 2015. Global Ocean Data Analysis Project, Version 2 (GLODAPv2),
1113 ORNL/CDIAC-162, NDP-093. Carbon Dioxide Information Analysis Center, Oak Ridge
1114 National Laboratory, US Department of Energy, Oak Ridge, Tennessee.
1115 doi:10.3334/CDIAC/OTG.NDP093_GLODAPv2

1116

1117 Lambert, S. and Boer, G.: CMIP1 evaluation and intercomparison of coupled climate models,
1118 Climate Dynamics, 17, 83-106, 10.1007/PL00013736, 2001.

1119

1120 Landry, M., Barber, R., Bidigare, R., Chai, F., Coale, K., Dam, H., Lewis, M., Lindley, S.,
1121 McCarthy, J., Roman, M., Stoecker, D., Verity, P., and White, J.: Iron and grazing constraints on
1122 primary production in the central equatorial Pacific: An EqPac synthesis, Limnology and
1123 Oceanography, 42, 405-418, 10.4319/lo.1997.42.3.0405, 1997.

1124

1125 Lauvset, S., Key, R., Olsen, A., van Heuven, S., Velo, A., Lin, X., Schirnick, C., Kozyr, A.,
1126 Tanhua, T., Hoppema, M., Jutterstrom, S., Steinfeldt, R., Jeansson, E., Ishii, M., Perez, F.,
1127 Suzuki, T., and Watelet, S.: A new global interior ocean mapped climatology: the 1 degrees x 1
1128 degrees GLODAP version 2, Earth System Science Data, 8, 325-340, 10.5194/essd-8-325-2016,
1129 2016.

1130

1131 Li, Y.: Distribution patterns of the elements in the ocean - a synthesis, Geochimica et
1132 Cosmochimica Acta, 55, 3223-3240, 1991.

1133

1134 Locarnini, R.A., Mishonov, A.V., Antonov, J.I., Boyer, T.P., Garcia, H.E., Baranova, O.K.,
1135 Zweng, M.M., and Johnson, D.R.: World Ocean Atlas 2009, Volume 1: Temperature. Levitus,
1136 S., Ed., NOAA Atlas NESDIS 68, 184 pp., 2010.

1137

1138 Locarnini, R.A., Mishonov, A.V., Baranova, O.K., Boyer, T.P., Zweng, M.M., Garcia, H.E.,
1139 Reagan, J.R., Seidov, D., Weathers, K., Paver, C.R., and Smolyar, I.: World Ocean Atlas 2018,
1140 Volume 1: Temperature. A. Mishonov Technical Ed., NOAA Atlas NESDIS 81, 52pp., 2018.

1141

1142 Loladze, I., Kuang, Y., and Elser, J.: Stoichiometry in producer-grazer systems: Linking energy
1143 flow with element cycling, Bulletin of Mathematical Biology, 62, 1137-1162,
1144 10.1006/bulm.2000.0201, 2000.

1145

1146 Lukas, R.: Pacific ocean equatorial currents, in: Encyclopedia of Ocean Sciences, edited by:
1147 Steele, J.H., Thorpe, S.A., and Turekian, K.K., Academic, San Diego, 2069-2076,
1148 10.1006/rwos.2001.0354, 2001.

1149

Madec, G. and Imbard, M.: A global ocean mesh to overcome the North Pole singularity, Climate Dynamics, 12, 381-388, 10.1007/s003820050115, 1996.

Moriarty, R. and O'Brien, T.: Distribution of mesozooplankton biomass in the global ocean, Earth System Science Data, 5, 45-55, 10.5194/essd-5-45-2013, 2013.

Nozaki, Y.: Elemental Distribution, in: Encyclopedia of Ocean Sciences, edited by: Steele, J.H., Thorpe, S.A., and Turekian, K.K., Academic, San Diego, 840-845, 10.1006/rwos.2001.0402, 2001.

Orr, J. C., Najjar, R. G., Aumont, O., Bopp, L., Bullister, J. L., Danabasoglu, G., Doney, S. C., Dunne, J. P., Dutay, J. C., Graven, H., Griffies, S. M., John, J. G., Joos, F., Levin, I., Lindsay, K., Matear, R. J., McKinley, G. A., Mouchet, A., Oschlies, A., Romanou, A., Schlitzer, R., Tagliabue, A., Tanhua, T., and Yool, A.: Biogeochemical protocols and diagnostics for the CMIP6 Ocean Model Intercomparison Project (OMIP), Geoscientific Model Development, 10, 2169-2199, 10.5194/gmd-10-2169-2017, 2017.

Philander, S.G. and Chao, Y.: On the contrast between the seasonal cycles of the equatorial Atlantic and Pacific oceans, Journal of Physical Oceanography, 21, 1399-1406, 1991.

Raven, J. and Geider, R.: Temperature and algal growth, New Phytologist, 110, 441-461, 10.1111/j.1469-8137.1988.tb00282.x, 1988.

Riche, O. and Christian, J.: Ocean dinitrogen fixation and its potential effects on ocean primary production in Earth system model simulations of anthropogenic warming, Elementa-Science of the Anthropocene, 6, 10.1525/elementa.277, 2018.

Schlitzer, R., Anderson, R., Dodas, E., Lohan, M., Geibere, W., Tagliabue, A., Bowie, A., Jeandel, C., Maldonado, M., Landing, W., Cockwell, D., Abadie, C., Abouchami, W., Achterberg, E., Agather, A., Aguliar-Islas, A., van Aken, H., Andersen, M., Archer, C., Auro, M., de Baar, H., Baars, O., Baker, A., Bakker, K., Basak, C., Baskaran, M., Bates, N., Bauch, D., van Beek, P., Behrens, M., Black, E., Bluhm, K., Bopp, L., Bouman, H., Bowman, K., Bown, J., Boyd, P., Boye, M., Boyle, E., Branellec, P., Bridgestock, L., Brissebrat, G., Browning, T., Bruland, K., Brumsack, H., Brzezinski, M., Buck, C., Buck, K., Buesseler, K., Bull, A., Butler, E., Cai, P., Mor, P., Cardinal, D., Carlson, C., Carrasco, G., Casacuberta, N., Casciotti, K., Castrillejo, M., Chamizo, E., Chance, R., Charette, M., Chaves, J., Cheng, H., Chever, F., Christl, M., Church, T., Closset, I., Colman, A., Conway, T., Cossa, D., Croot, P., Cullen, J., Cutter, G., Daniels, C., Dehairs, F., Deng, F., Dieu, H., Duggan, B., Dulaquais, G., Dumousseaud, C., Echegoyen-Sanz, Y., Edwards, R., Ellwood, M., Fahrbach, E., Fitzsimmons, J., Flegal, A., Fleisher, M., van de Flierdt, T., Frank, M., Friedrich, J., Fripiat, F., Frollje, H., Galer, S., Gamo, T., Ganeshram, R., Garcia-Orellana, J., Garcia-Solsona, E., Gault-Ringold, M., George, E., Gerringa, L., Gilbert, M., Godoy, J., Goldstein, S., Gonzalez, S., Grissom, K., Hammerschmidt, C., Hartman, A., Hassler, C., Hathorne, E., Hatta, M., Hawco, N., Hayes, C., Heimburger, L., Helgoe, J., Heller, M., Henderson, G., Henderson, P., van Heuven, S., Ho, P., Horner, T., Hsieh, Y., Huang, K., Humphreys, M., Isshiki, K., Jacquot, J., Janssen, D., Jenkins, W., John, S., Jones, E., Jones, J., Kadko, D., Kayser, R., Kenna, T., Khondoker, R., Kim, T.,

Kipp, L., Klar, J., Klunder, M., Kretschmer, S., Kumamoto, Y., Laan, P., Labatut, M., Lacan, F., Lam, P., Lambelet, M., Lamborg, C., Le Moigne, F., Le Roy, E., Lechtenfeld, O., Lee, J., Lherminier, P., Little, S., Lopez-Lora, M., Lu, Y., Masque, P., Mawji, E., Mcclain, C., Measures, C., Mehic, S., Menzel Barraqueta, J., van der Merwe, P., Middag, R., Mieruch, S., Milne, A., Minami, T., Moffett, J., Moncoiffe, G., Moore, W., Morris, P., Morton, P., Nakaguchi, Y., Nakayama, N., Niedermiller, J., Nishioka, J., Nishiuchi, A., Noble, A., Obata, H., Ober, S., Ohnemus, D., van Ooijen, J., O'Sullivan, J., Owens, S., Pahnke, K., Paul, M., Pavia, F., Pena, L., Petersh, B., Planchon, F., Planquette, H., Pradoux, C., Puigcorbe, V., Quay, P., Queroue, F., Radic, A., Rauschenberg, S., Rehkamper, M., Rember, R., Remenyi, T., Resing, J., Rickli, J., Rigaud, S., Rijkenberg, M., Rintoul, S., Robinson, L., Roca-Marti, M., Rodellas, V., Roeske, T., Rolison, J., Rosenberg, M., Roshan, S., van der Loaff, M., Ryabenko, E., Saito, M., Salt, L., Sanial, V., Sarthou, G., Schallenberg, C., Schauer, U., Scher, H., Schlosser, C., Schnetger, B., Scott, P., Sedwick, P., Semiletov, I., Shelley, R., Sherrell, R., Shiller, A., Sigman, D., Singh, S., Slagter, H., Slater, E., Smethie, W., Snaith, H., Sohrin, Y., Sohst, B., Sonke, J., Speich, S., Steinfeldt, R., Stewart, G., Stichel, T., Stirling, C., Stutsman, J., Swarr, G., Swift, J., Thomas, A., Thorne, K., Till, C., Till, R., Townsend, A., Townsend, E., Tuerena, R., Twining, B., Vance, D., Velazquez, S., Venchiarutti, C., Villa-Alfageme, M., Vivancos, S., Voelker, A., Wake, B., Warner, M., Watson, R., van Weerlee, E., Weigand, M., Weinstein, Y., Weiss, D., Wisotzki, A., Woodward, E., Wu, J., Wu, Y., Wuttig, K., Wyatt, N., Xiang, Y., Xie, R., Xue, Z., Yoshikawa, H., Zhang, J., Zhang, P., Zhao, Y., Zheng, L., Zheng, X., Zieringer, M., Zimmer, L., Ziveri, P., Zunino, P., and Zurbrick, C.: The GEOTRACES Intermediate Data Product 2017, Chemical Geology, 493, 210-223, 10.1016/j.chemgeo.2018.05.040, 2018.

Séférian, R., Gehlen, M., Bopp, L., Resplandy, L., Orr, J., Marti, O., Dunne, J., Christian, J., Doney, S., Ilyina, T., Lindsay, K., Halloran, P., Heinze, C., Segschneider, J., Tjiputra, J., Aumont, O., and Romanou, A.: Inconsistent strategies to spin up models in CMIP5: implications for ocean biogeochemical model performance assessment, Geoscientific Model Development, 9, 1827-1851, 10.5194/gmd-9-1827-2016, 2016.

Siegel, D., Buesseler, K., Behrenfeld, M., Benitez-Nelson, C., Boss, E., Brzezinski, M., Burd, A., Carlson, C., D'Asaro, E., Doney, S., Perry, M., Stanley, R., and Steinberg, D.: Prediction of the Export and Fate of Global Ocean Net Primary Production: The EXPORTS Science Plan, Frontiers in Marine Science, 3, 10.3389/fmars.2016.00022, 2016.

Steinacher, M., Joos, F., Frolicher, T., Bopp, L., Cadule, P., Cocco, V., Doney, S., Gehlen, M., Lindsay, K., Moore, J., Schneider, B., and Segschneider, J.: Projected 21st century decrease in marine productivity: a multi-model analysis, Biogeosciences, 7, 979-1005, 10.5194/bg-7-979-2010, 2010.

Stramski, D., Reynolds, R., Babin, M., Kaczmarek, S., Lewis, M., Rottgers, R., Sciandra, A., Stramska, M., Twardowski, M., Franz, B., and Claustre, H.: Relationships between the surface concentration of particulate organic carbon and optical properties in the eastern South Pacific and eastern Atlantic Oceans, Biogeosciences, 5, 171-201, 10.5194/bg-5-171-2008, 2008.

Strous, M., Heijnen, J., Kuenen, J., and Jetten, M.: The sequencing batch reactor as a powerful tool for the study of slowly growing anaerobic ammonium-oxidizing microorganisms, Applied

Microbiology and Biotechnology, 50, 589-596, 10.1007/s002530051340, 1998.

Swart, N., Cole, J., Kharin, V., Lazare, M., Scinocca, J., Gillett, N., Anstey, J., Arora, V., Christian, J., Hanna, S., Jiao, Y., Lee, W., Majaess, F., Saenko, O., Seiler, C., Seinen, C., Shao, A., Sigmond, M., Solheim, L., von Salzen, K., Yang, D., and Winter, B.: The Canadian Earth System Model version 5 (CanESM5.0.3), Geoscientific Model Development, 12, 4823-4873, 10.5194/gmd-12-4823-2019, 2019a.

Swart, N. C., Cole, J., Kharin, S., Lazare, M., Scinocca, J., Gillett, N., Anstey, J., Arora, V., Christian, J., Hanna, S., Jiao, Y., Lee, W., Majaess, F., Saenko, O., Seiler, C., Seinen, C., Shao, A., Solheim, L., von Salzen, K., Yang, D., and Winter, B.: The Canadian Earth System Model (CanESM), v5.0.3., https://doi.org/10.5281/zenodo.3251114, 2019b.

Takeda, S., Chai, F., and Nishioka, J., Eds.: Report of Working Group 22 on Iron Supply and its Impact on Biogeochemistry and Ecosystems in the North Pacific Ocean. PICES Sci. Rep. No. 42, 60 pp., 2013.

Taylor, K.: Summarizing multiple aspects of model performance in a single diagram., Journal of Geophysical Research-Atmospheres, 106, 7183-7192, 10.1029/2000JD900719, 2001.

Tesdal, J., Christian, J., Monahan, A., and von Salzen, K.: Evaluation of diverse approaches for estimating sea-surface DMS concentration and air-sea exchange at global scale, Environmental Chemistry, 13, 390-412, 10.1071/EN14255, 2016.

von Salzen, K., Scinocca, J. F., McFarlane, N. A., Li, J. N., Cole, J. N. S., Plummer, D., Verseghy, D., Reader, M. C., Ma, X. Y., Lazare, M., and Solheim, L.: The Canadian Fourth Generation Atmospheric Global Climate Model (CanAM4). Part I: Representation of Physical Processes, Atmosphere-Ocean, 51, 104-125, 10.1080/07055900.2012.755610, 2013.

Wolf-Gladrow, D., Zeebe, R., Klaas, C., Kortzinger, A., and Dickson, A.: Total alkalinity: The explicit conservative expression and its application to biogeochemical processes, Marine Chemistry, 106, 287-300, 10.1016/j.marchem.2007.01.006, 2007.

Zahariev, K., Christian, J., and Denman, K.: Preindustrial, historical, and fertilization simulations using a global ocean carbon model with new parameterizations of iron limitation, calcification, and N_2 fixation, Progress in Oceanography, 77, 56-82, 10.1016/j.pocean.2008.01.007, 2008.

Zweng, M.M., Reagan, J.R., Seidov, D., Boyer, T.P., Locarnini, R.A., Garcia, H. E., Mishonov, A.V., Baranova, O.K., Weathers, K., Paver, C.R., and Smolyar, I.: World Ocean Atlas 2018, Volume 2: Salinity. A. Mishonov Technical Ed., NOAA Atlas NESDIS 82, 50pp., 2018.